Supporting Information

Bio-inspired engineering of Bi_2S_3-PPy composite for efficient electrocatalytic reduction of carbon dioxide

Chengjin Li[a], Zhengzheng Liu[c], Xiaoxia Zhou[a,*], Lifang Zhang[a], Zhengqian Fu[a], Yiji Wu[a], XiMeng Lv[c], Gengfeng Zheng[c*], Hangrong Chen[a,b*]

[a.] State Key Laboratory of High Performance Ceramics and Superfine Microstructure, Shanghai Institute of Ceramics, Chinese Academy of Science, 1295 DingXi Road, Shanghai 200050, China.

[b.] School of Chemistry and Materials Science, Hangzhou Institute for Advanced Study, University of Chinese Academy of Sciences, 1 Sub-lane Xiangshan, Hangzhou 310024, China.

[c.] Laboratory of Advanced Materials, Department of Chemistry and Shanghai Key Laboratory of Molecular Catalysis and Innovative Materials Faculty of Chemistry and Materials Science, Fudan University, Shanghai 200438, China.

* E-mail: zhouxiaoxia@mail.sic.ac.cn;
gfzheng@fudan.edu.cn;
hrchen@mail.sic.ac.cn;

Experimental Details

Chemicals and materials.

Bismuth nitrate pentahydrate ($Bi(NO_3)_3•5H_2O$, ≥99%), Thiourea (CH_4N_2S, ≥99%), Polyvinylpyrrolidone ($(C_6H_9NO)_n$, K30), acetone (99.7%), $KHCO_3$ (99.9%), KOH (99.9%), Pyrrole (99%), $FeCl_3•6H_2O$ (99%), commercial Bi_2S_3 (99.9%), RuO_2 (99.9%), and IrO_2 (99.9%) were all purchased from Aladdin Co. Ltd. (Shanghai, China), ethanol (C_2H_5OH, ≥97%) was purchased from Sinopharm Chemical Reagent Co. Ltd. (Shanghai, China). The Nafion solution (Dupont, D-520 dispersion, 5% w/w in water, and 1-propanol) was purchased from Alfa Aesar. The gas diffusion layer was purchased from Fuel Cell Store. Hydroxide exchange membranes FAB-PK-130 were purchased from Fumatech. CO_2 gas (99.99%), Ar gas (99.99%), and all the standard gases for gas chromatography were purchased from Shanghai Tomoe Gas Company. All the chemicals were used without further purification. Ultrapure Millipore water (18.2 MΩ) was used in all experiments.

Synthesis of Bi_2S_3 urchin-like assembly.

In a typical synthesis, PVP (0.5 g) and thiourea (0.3 g) were dispersed in 60 mL of EG under continuous stirring at 65 ℃. Then, to this suspension, 10 mL of 0.1 M $Bi(NO_3)_3$ solution (in ethylene glycol) was added dropwise. After 30 min of further stirring, the mixed suspension was transferred to a Teflon-lined autoclave and kept at 140 ℃ for 8 h. The resultant black precipitate was collected by centrifugation, washed thoroughly with deionized water and ethanol, and dried in a vacuum at 60 ℃ overnight. Bi_2S_3-PPy without the addition of PVP was synthesized with the same procedure as that of urchin-like Bi_2S_3 except without adding PVP.

Synthesis of Bi_2S_3-PPy composite.

The resulting Bi_2S_3 power (0.15 g) was immersed in $FeCl_3$ aqueous solution (0.2 mL, 0.1 M) and dried in a vacuum. The dry powder and pyrrole monomer (2 mL) were separately placed in two vials, which were then sealed in a bottle filled with argon and kept at 40 ℃ for 3 h. The Bi_2S_3-PPy-1 h and Bi_2S_3-PPy-5 h were formed by adjusting reaction time 1 h and 5 h, respectively. In addition, the com-Bi_2S_3-PPy and Bi_2S_3-PPy

without the addition of PVP were synthesized with the same procedure as that of Bi_2S_3-PPy.

Preparation of working electrodes.

The substrate electrode was fabricated by carbon paper (1 x 0.5 cm), which was sonicated in hydrochloric acid (1.0 M), acetone, and deionized water for 30 min, respectively. Typically, power catalysts (10 mg) and carbon black (5 mg) were dispersed in Nafion perfluorinated resin solution (5%, 50 μL), ethanol (500 μL), and deionized water (500 μL) by ultrasonication for 30 min to form homogeneous catalysts ink. Then the as-prepared catalyst ink was onto the carbon paper several times with a pipette (100 μL), using 30 μL for each electrode. Finally, the obtained composite electrodes were dried at room temperature for 12 h.

Electrochemical measurements.

All the electrochemical experiments were performed in a gas-tight H-cell containing 30 mL of electrolyte, which was separated by a proton exchange membrane (Nafion N115). The Ag/AgCl (saturated KCl) and Pt plate (1.5 x 1.5 cm^2) were used as the reference and counter electrodes, respectively. Electrochemical data were recorded on a Biologic electrochemical workstation. Before each experiment, CO_2 (99.999%) was continuously bubbled into the electrolyte for 30 mins to eliminate O_2 and saturate the electrolyte with CO_2. The electrochemical experiments were measured at room temperature (25 ± 3 °C), and all potentials reported in this paper are referenced to a reversible hydrogen electrode (RHE, $E_{RHE} = E_{Ag/AgCl} + 0.197 + 0.0591 \times pH$). The pH of the Ar/$CO_2$-saturated 0.5 M $KHCO_3$ electrolyte is 8.56 and 7.33 in this study.

Products analysis.

The gaseous products of CO_2 electrocatalytic reduction were monitored by gas chromatography (GC) (Thermo Scientific Trace 1300) equipped with thermal conductivity (TCD) and flame ionization detector (FID). Quantification of the products was performed by an external standard method.

CO and H_2 Faradaic efficiency (FE) can be computed as:

$$FE = \frac{Fn\alpha}{Q}$$

Where F is the Faraday constant, $\alpha = 2$ is the number of electrons involved in the electrode reaction, n is the amount of CO、H_2 produced, and Q is the total charge consumed during the whole electrolysis.

The $KHCO_3$ solution after electrolysis was collected and analyzed on a Bruker Ascend 500 MHz NMR spectrometer to quantify liquid products. The quantification of the liquid products was obtained as follows. The molar quantity of formate (N_{formate}) was measured via the internal standard method of ^{1}H NMR. Typically, 10 mL of electrolyte was mixed with 50 μL of 50 mM DMSO solution by mixing 250 μL above solution with 350 μL D_2O. The ^{1}H NMR spectrum was measured with water suppression via a pre-saturation method. The area ratio of the formate peak to the DMSO peak was compared to the standard curve to quantify the concentration of formate. The N_{formate} was calculated by multiplying the concentration of formate with the volume of electrolyte in the cathode.

$$\text{FE} = \frac{\alpha n F}{Q}$$

Where α is the electron transferred to produce formate ($\alpha = 2$), n is the amount of formate produced, F is the Faradaic constant, and Q is the total charge consumed during the whole electrolysis.

The energy efficiency for the conversion of CO_2 into formate was calculated by the following equation.

$$\Phi_{formate} = \frac{FE * \Delta E^{0}_{formate}}{\Delta E_{formate}}$$

$\Phi_{formate}$ was the energy efficiency for the conversion of CO_2 into formate. $\Delta E^{0}_{formate}$was the difference between the standard half reaction potentials for water oxidation (1.23 V *vs*. RHE) and the reduction of CO_2 into formate (-0.2 V *vs*. RHE). $\Delta E_{formate}$was the difference between the standard water oxidation potential and the working potential at the cathode, respectively.

Linear sweep voltammetry (LSV) was carried out in CO_2-saturated or Ar-saturated 0.5 M $KHCO_3$ electrolyte with a scan rate of 50 mV s^{-1}. The cyclic voltammetry

measurement was conducted in CO_2-saturated 0.5 M $KHCO_3$ solution using a three-electrode cell equipped with an Ag/AgCl reference electrode and a Pt foil counter electrode at 25 °C. Electrochemical impedance spectroscopy (EIS) was recorded at -0.9 V *vs*. RHE in CO_2-saturated 0.5 M $KHCO_3$ electrolyte with an amplitude of 5 mV, and the frequency range is from 0.1 Hz to 1000000 Hz. The Tafel plot (overpotential versus log $j_{formate}$) was derived from the controlled potential electrolysis results. Double-layer capacitance (C_{dl}) was determined by measuring the capacitive current associated with double-layer charging from the scan-rate dependence of cyclic voltammogram (CV). The CV range from -0.1 V to 0 V *vs*. RHE. The C_{dl} was estimated by plotting the Δj ($\Delta j = j_a - j_c$) at -0.05 V *vs*. RHE against the scan rates, in which the j_a and j_c were the anodic and cathodic current densities, respectively. Electroreduction of CO_2 was investigated for 20 C at each applied potential by the controlled potential electrolysis method. Before each new electrocatalyst test, 100 cycles of cyclic voltammetry (CV) were used to activate the electrodes.

Flow cell measurements.

Preparation of electrode. For flow-cell CO_2 electrolysis, gas-diffusion-electrodes (GDEs) were prepared via drop-casting catalysts onto a gas-diffusion-layer (GDL, Freudenberg). To prepare the cathode electrode, a well-dispersed catalyst slurry comprising 3 mg of catalyst, 0.5 mL of acetone, and 20 μL of Nafion ionomer solution was mixed. Next, the catalyst slurry was slowly drop-casted onto a GDL to attain a catalyst loading of ~ 1 mg cm^{-2}. A similar procedure was used for RuO_2/IrO_2 nanoparticles (99% metal basis, Macklin) to prepare the anode electrode.

Electrochemical analysis of CO_2 reduction. For CO_2 electroreduction (CO_2RR) in flow-cell, the electrochemical tests were conducted using a 1-cm^2 flow cell on a CHI 750E electrochemical workstation at room temperature (25 ± 1 °C). The flow cell configuration consisted of a catalyst-sprayed GDE as the working electrode, an IrO_2-sprayed GDE as the anode, and an anion exchange membrane (Fumatech FAB-PK-130) to separate the cathode and anode chambers. All applied potentials were converted to the RHE scale according to the Nernst equation:

$$E_{RHE}(V) = E_{Ag/AgCl}(V) + 0.197\ V + 0.059 \times pH$$

The reaction was performed in 1 M KOH as the electrolyte with a steady stream of CO_2 (30 s.c.c.m). The gas product was collected and analyzed by gas chromatography (Shanghai Ramiin GC 2060) and liquid products were quantified by ^1H nuclear magnetic resonance (NMR) spectroscopy (Bruker AVANCEAV III HD 500) and the pre-saturation method was used to suppress water peak.

The CO_2-OER electrolysis was carried out in a two-electrode system. The Bi_2S_3-PPy and commercial RuO_2 served as CO_2RR catalyst and OER catalyst, respectively. And the 0.5 M $KHCO_3$ and 1M KOH respectively served as the catholyte and anolyte, separated by a bipolar membrane. Other test conditions were similar to the CO_2RR process in an H-type electrolyzer.

Zn-CO_2 measurements

The Zn-CO_2 batteries applied H-cell configurations. The gas diffusion layer loading Bi_2S_3-PPy and Zn plate served as battery electrodes. The 2 M $KHCO_3$ + 0.02 M HCOOH and 2 M KOH + 0.02 M $Zn(AC)_2$ served as electrolytes, which were separated by a bipolar membrane.

The cathodic and anodic reactions of the aqueous rechargeable Zn-CO_2 battery during the charge and discharge processes.

1) When the aqueous Zn-CO_2 battery discharge, the following reactions are assumed to take place:

Cathode (CO_2-saturated 0.5 M KCO_3, pH = 7.3)

$CO_2 + 2e^- + 2H^+ \rightarrow HCOOH$

Anode (0.8 M KOH with 0.02 M $Zn(CH_3COO)_2$)

$Zn \rightarrow Zn^{2+} + 2e^-$

$Zn^{2+} + 4OH^- \rightarrow Zn(OH)^{2-}_4$

Overall discharge reaction:

$Zn + CO_2 + 2H^+ + 4OH^- \rightarrow Zn(OH)^{2-}_4 + HCOOH$

2) When aqueous Zn-CO_2 battery discharge, the following reactions are assumed to take place:

Cathode:

$H_2O \rightarrow 1/2O_2 + 2H^+ + 2e^-$

Anode:

$Zn(OH)^{2-}_4 \rightarrow Zn^{2+} + 4OH^-$

$Zn^{2+} + 2e^- \rightarrow Zn$

Overall charge reaction:

$Zn(OH)^{2-}_4 + H_2O \rightarrow Zn + 1/2O_2 + 2H^+ + 4OH^-$

In situ electrochemical Raman measurements were performed by a tailor-made flow cell. A peristaltic pump was used to pump 0.5 M $KHCO_3$ electrolyte at a constant flow rate of 3 mL min^{-1} over the Bi_2S_3-PPy supported GDL electrode. CO_2 gas was introduced to the back of GDL in a gas chamber at a flow rate of 10 s.c.c.m. During in situ Raman measurements, the Raman spectra were recorded against the applied potential range of -0.1 to -1.5 V *vs*. RHE at a Renishaw Via Raman spectrometer (λ = 633 nm).

In situ ATR-IR measurements were conducted by a Nicolet 6700 infrared spectrometer equipped with a liquid nitrogen-cooled MCT detector. The spectral resolution was set to 4.0 cm^{-1}, and a total of 64 interferograms were added to each spectrum. The spectrum was given in absorbance units defined as Abs = -lg (R/R_0), where R and R_0 represent the reflected in-situ ATR-IR intensities, corresponding to the single beam spectra of the sample and reference, respectively. The electrocatalyst was dropped on the 6 mm glassy carbon electrode and used as the working electrode for the in-situ ATR-IR test with a loading amount of 0.1 mg cm^{-2}. In all tests, the Pt electrode and Ag/AgCl electrode were used as counter electrode and reference electrode, respectively. The 0.5 M $KHCO_3$ solution saturated with CO_2 was used as the electrolyte. In this experiment, the chronopotentiometry test was used at different potentials without in-situ ATR-IR correction. The potential was set from open potential to -1.2 V *vs*. RHE, which was collected during the test. The electric potential of the reference single beam spectrum was open potential.

Physical characterizations.

Scanning electron microscopy (SEM) images were taken using the Magellan 400 high-resolution electron microscope. Transmission electron microscopy (TEM) was performed on a JEM-1400 transmission electron microcopy operated at 120 kV

accelerating voltage. High-resolution TEM (HRTEM) and high-angle annular dark-field scanning transmission electron microscopy (HAADF-STEM) images and elemental mappings were collected by the Tecnai G2 F20 field-emission transmission electron microscope. Fourier transforms (FT)-IR spectra were performed on the FT-IR spectrometer (Bruker Alpha II) with a KBr disk containing the catalysts powder. X-Ray diffraction (XRD) patterns were recorded on a Bruker D2 Phaser X-Ray powder Diffractometer with (Cu Kα radiation, $\lambda = 0.154$ nm). X-ray photoelectron spectroscopy (XPS) was recorded on the ESCAlab250 spectrometer. All the binding energy corresponds to the standard C1s peak at 284.8 eV in this experiment. Raman spectra were collected by a Renishaw in Via Raman microscope with a REM Laser at a wavelength of 532 nm. CO_2 adsorption isotherms were determined by Micromeritics ASAP 2020M at 25 ℃, and before the CO_2 adsorption experiment, two cycles of gas desorption were performed. The contact angle was measured by a contact-angle system (Biolin Scientific, Finland). TPD profiles of the samples were recorded by an AutoChem 2920 chemisorption analyzer with a TCD. Ultraviolet photoelectron spectroscopy (UPS) tests with photo energy of 21.22 eV were performed at EscaLab 250xi. The work functions of Bi_2S_3-PPy and Bi_2S_3 were determined by the difference in the photo energy and the binding energy of the secondary cutoff edge.

Density functional theory calculation details.

All the calculations are performed in the framework of the density functional theory (DFT) with the projector augmented plane-wave method, as implemented in the Vienna ab initio simulation package.[1] The generalized gradient approximation proposed by Perdew, Burke, and Ernzerhof (PBE) is selected for the exchange-correlation potential.[2] The long-range van der Waals interaction is described by the DFT-D3 approach.[3] The cut-off energy for the plane wave is set to 400 eV. The energy criterion is set to 10^{-5} eV in the iterative solution of the Kohn-Sham equation. A vacuum layer of 15 Å is added perpendicular to the sheet to avoid artificial interaction between periodic images. The Brillouin zone integration is performed using a 2 x 2 x 1 k-mesh. All the structures are relaxed until the residual forces on the atoms have declined to less than 0.03 eV/Å. The interface was constructed by

Bi_2S_3 (211) and Bi (110), where the lattice matching was performed by the package of structures of alloy generation and recognition.[4] Several S atoms were removed to investigate the absorption ability effect of this interface. The Gibbs free energy is calculated as follows: $\Delta G = E_{DFT} + E_{ZPE} - T\Delta S$, where E_{DFT} is the total energy from DFT calculations, E_{ZPE} is zero-point energy to correct the molecular vibration effect, and $T\Delta S$ is an entropic contribution to consider the thermal effect.

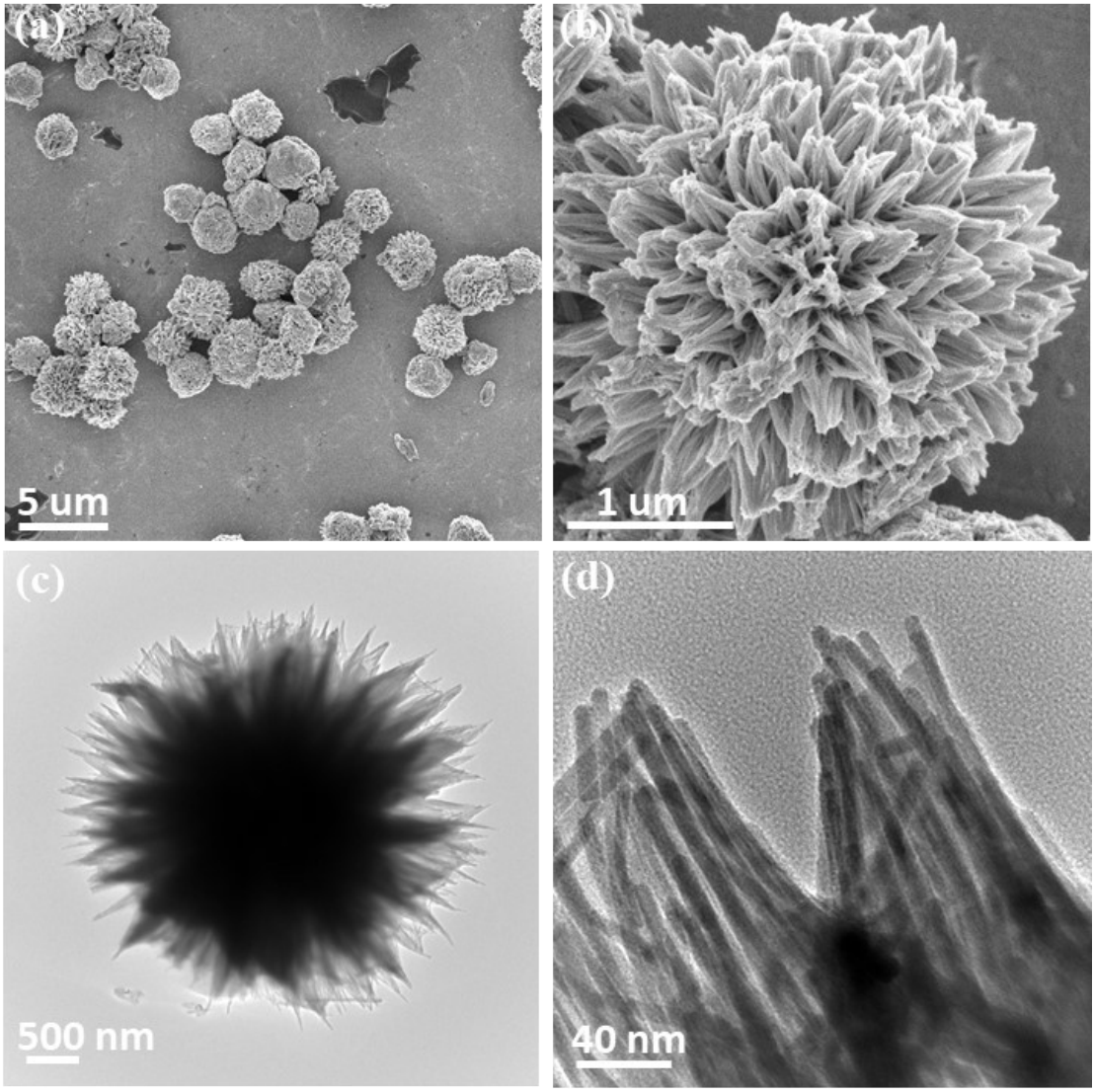

Figure S1. SEM images (a-b) and TEM images (c-d) of Bi_2S_3 with PVP additive.

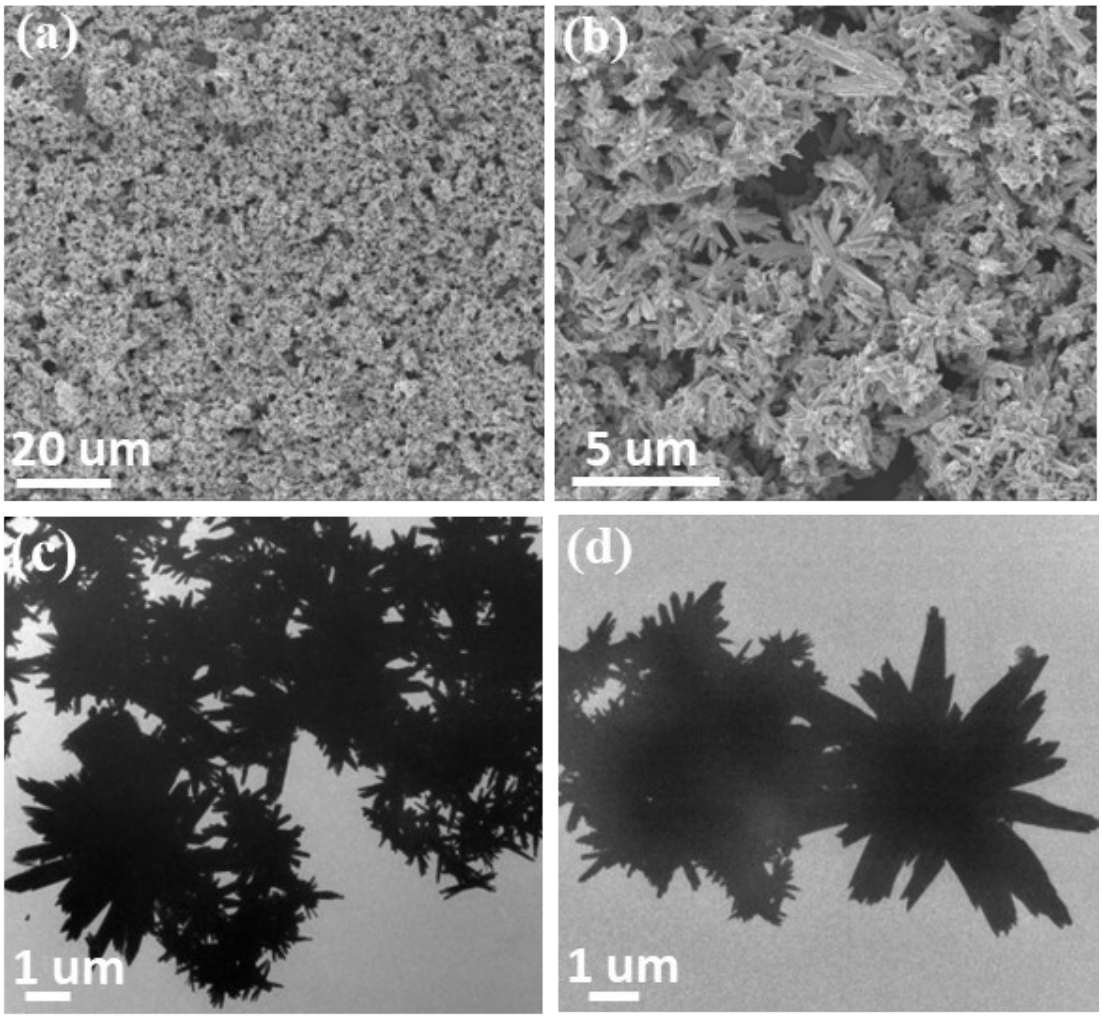

Figure S2. (a-b) Different magnification SEM images and (c-d) TEM images of Bi_2S_3 samples without PVP additive.

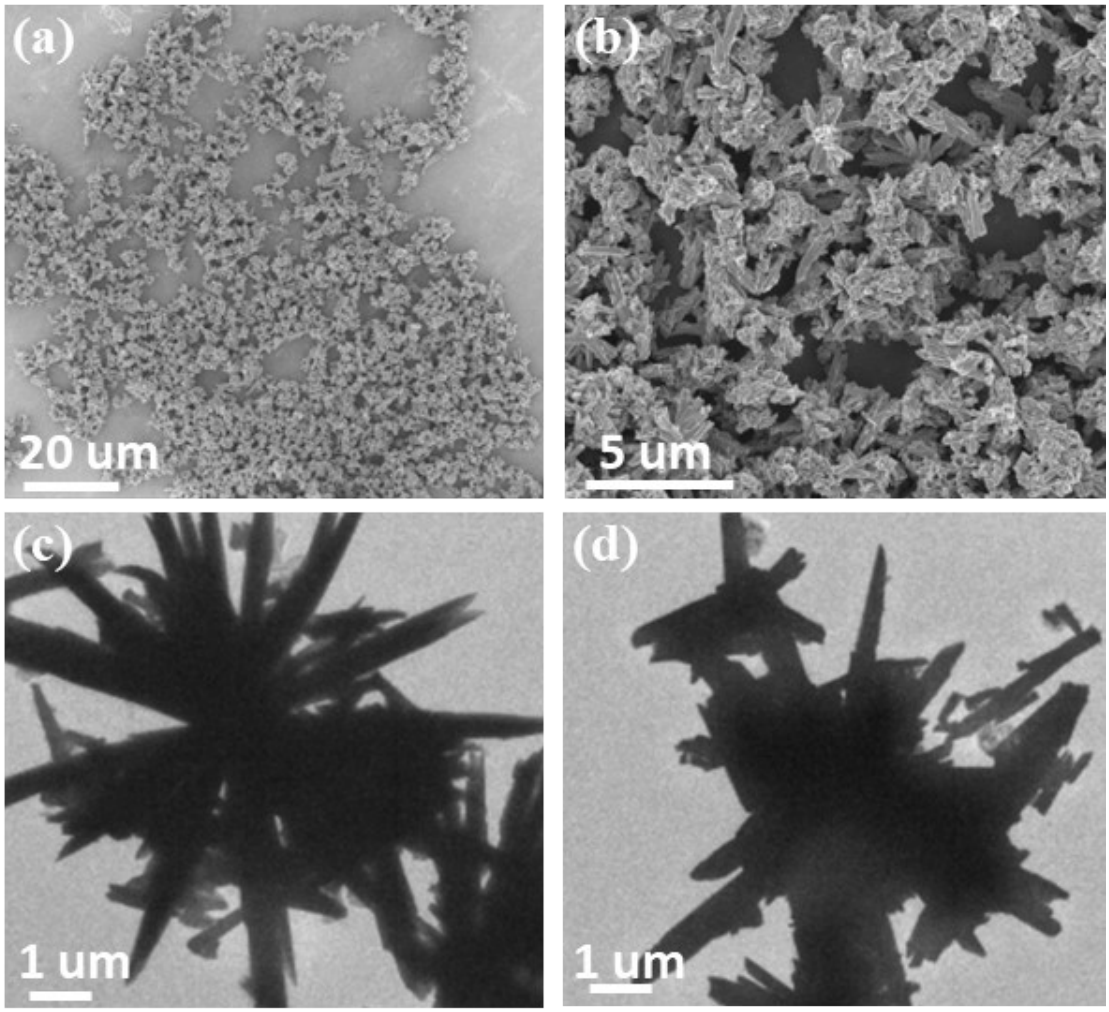

Figure S3. (a-b) Different magnification SEM images and (c-d) TEM images of Bi_2S_3-PPy sample without PVP additive.

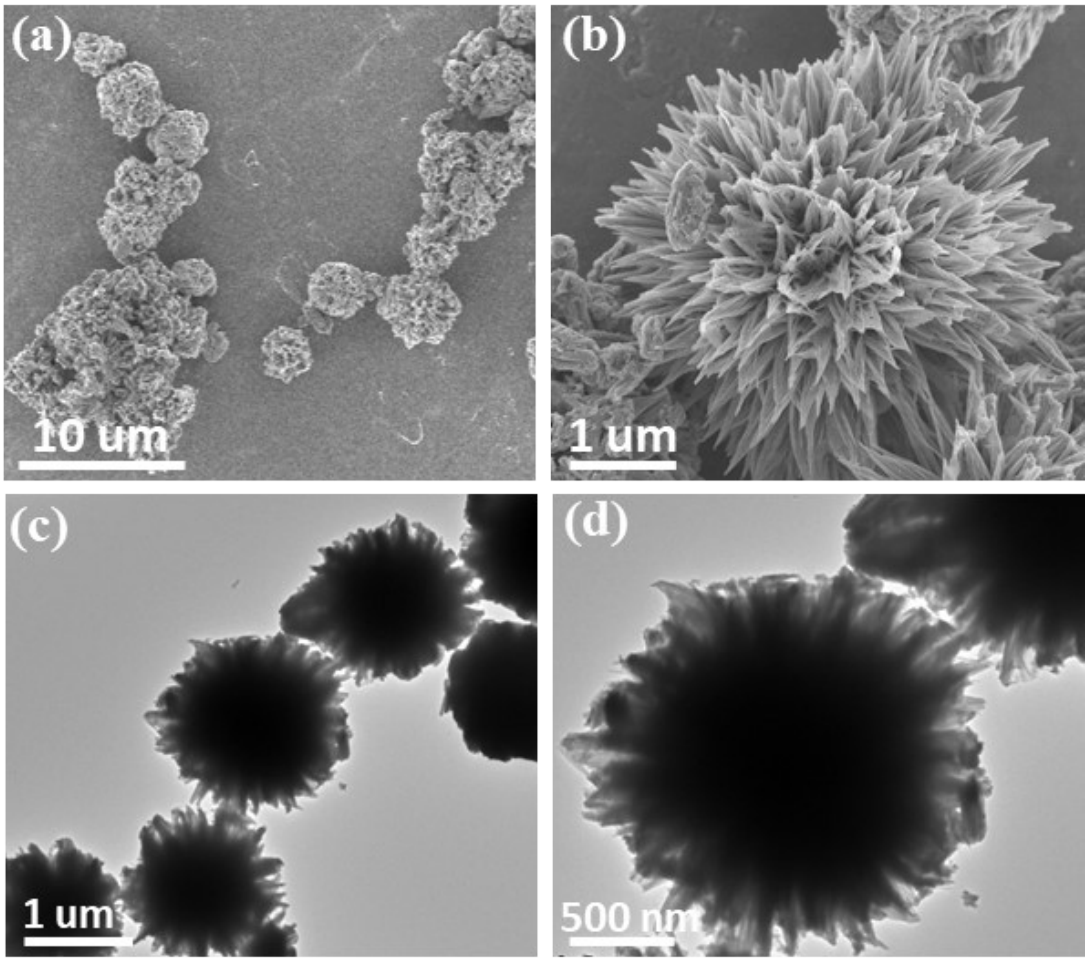

Figure S4. SEM images (a-b) and TEM images (c-d) of Bi_2S_3-PPy-1 h.

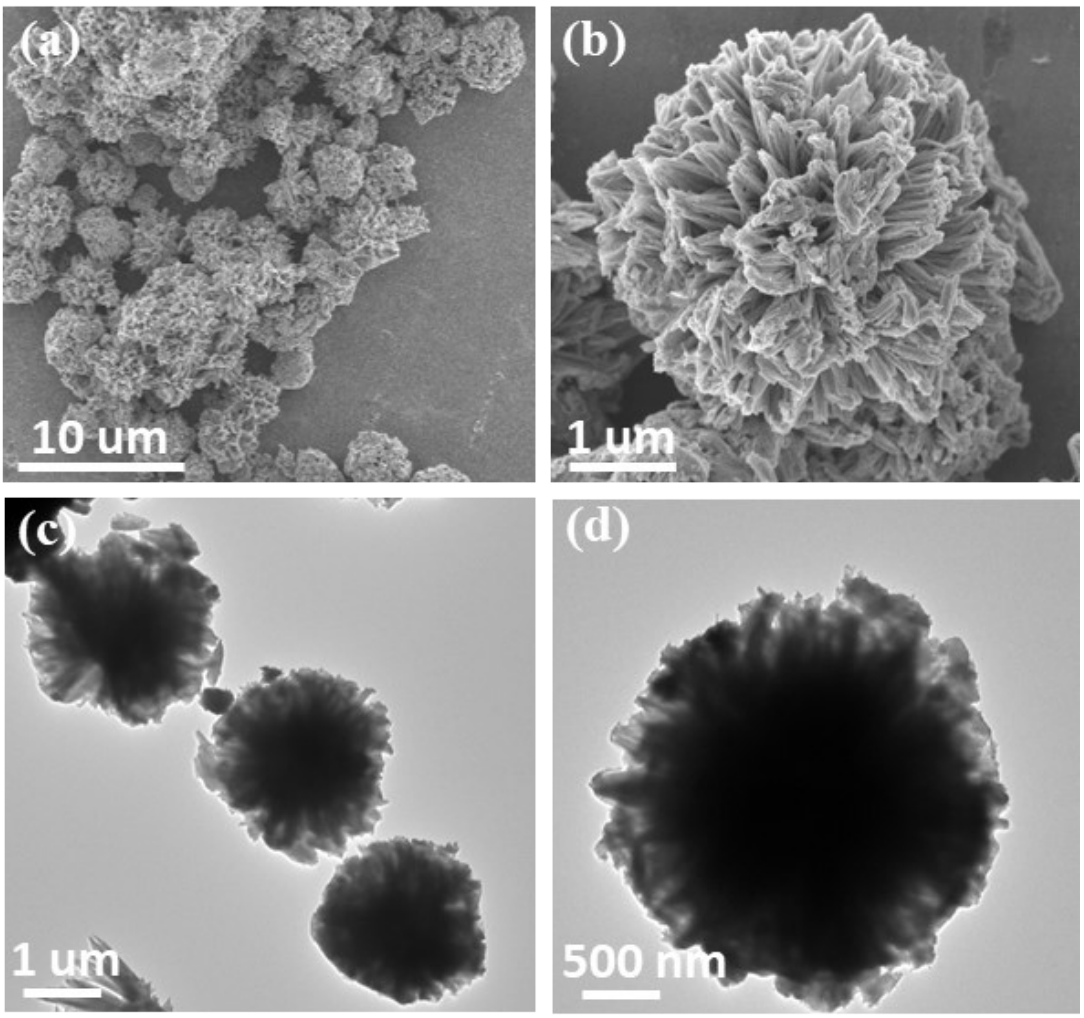

Figure S5. SEM images (a-b) and TEM images (c-d) of Bi_2S_3-PPy -5 h.

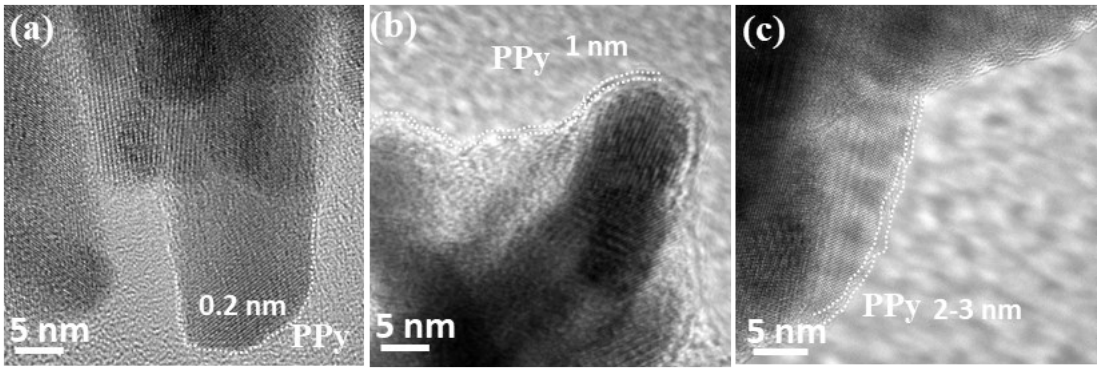

Figure S6. HRTEM images of (a) Bi_2S_3-PPy-1 h, (b) Bi_2S_3-PPy and (c) Bi_2S_3-PPy-5 h.

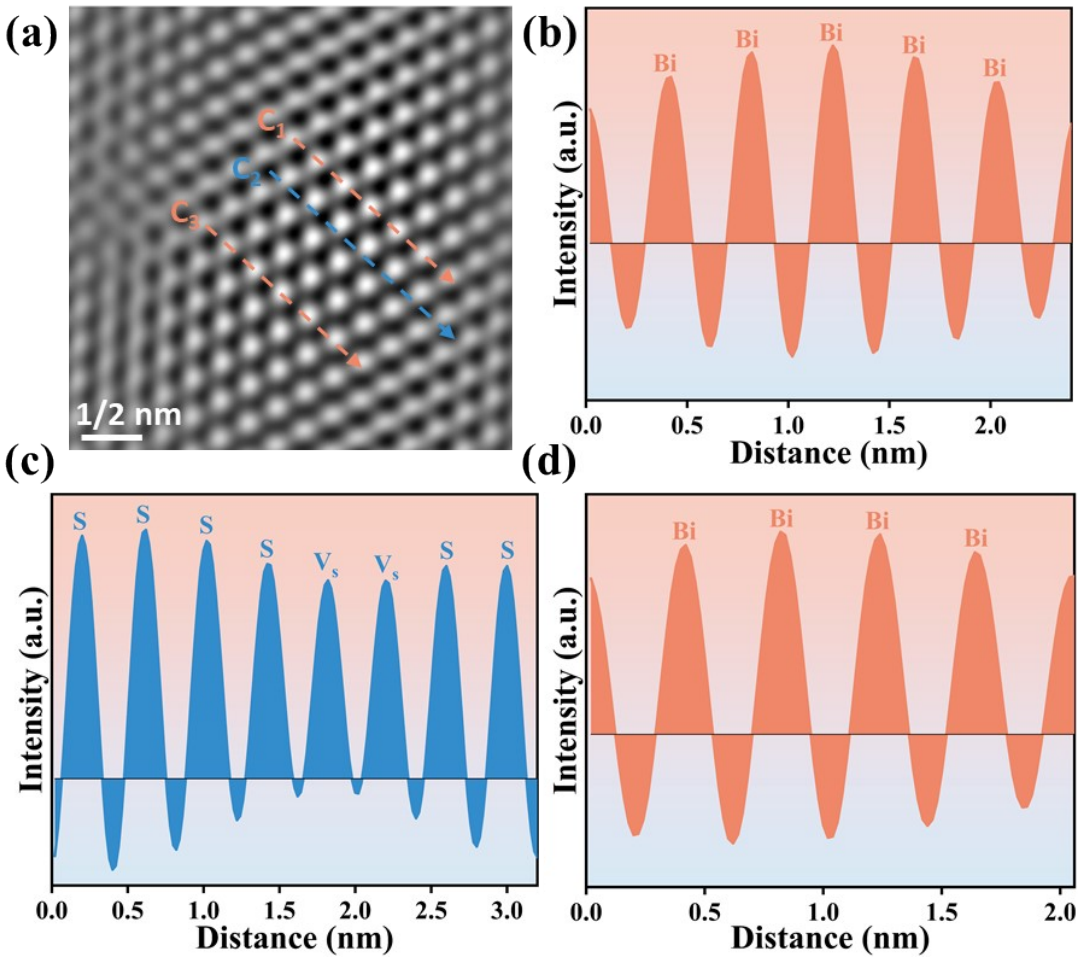

Figure S7. (a) Gaussian filter noise reduction image of the magnified HRTEM Bi_2S_3 image, (b-d) Intensity profiles of the lattice fringe corresponding to the dotted arrow in (a).

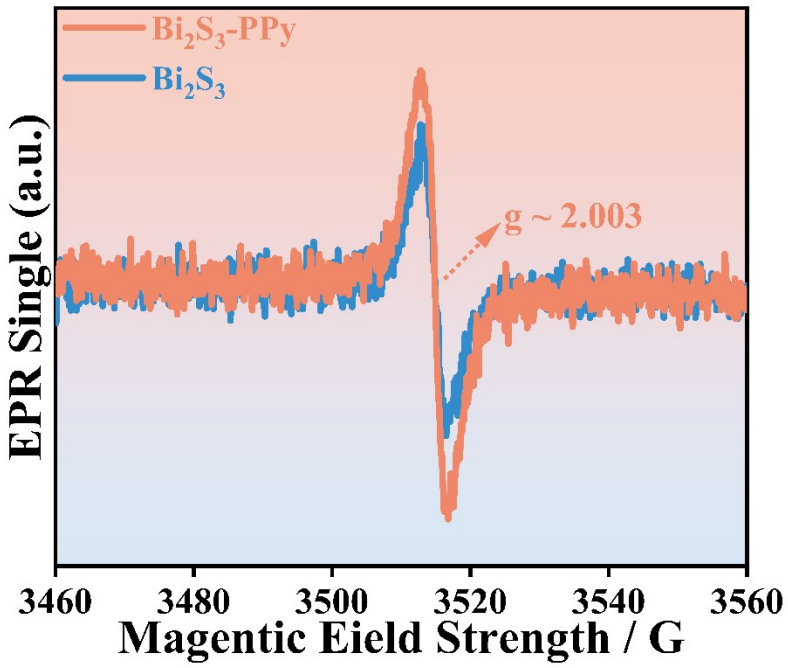

Figure S8. Electron paramagnetic resonances (EPR) spectra of Bi_2S_3-PPy and Bi_2S_3.

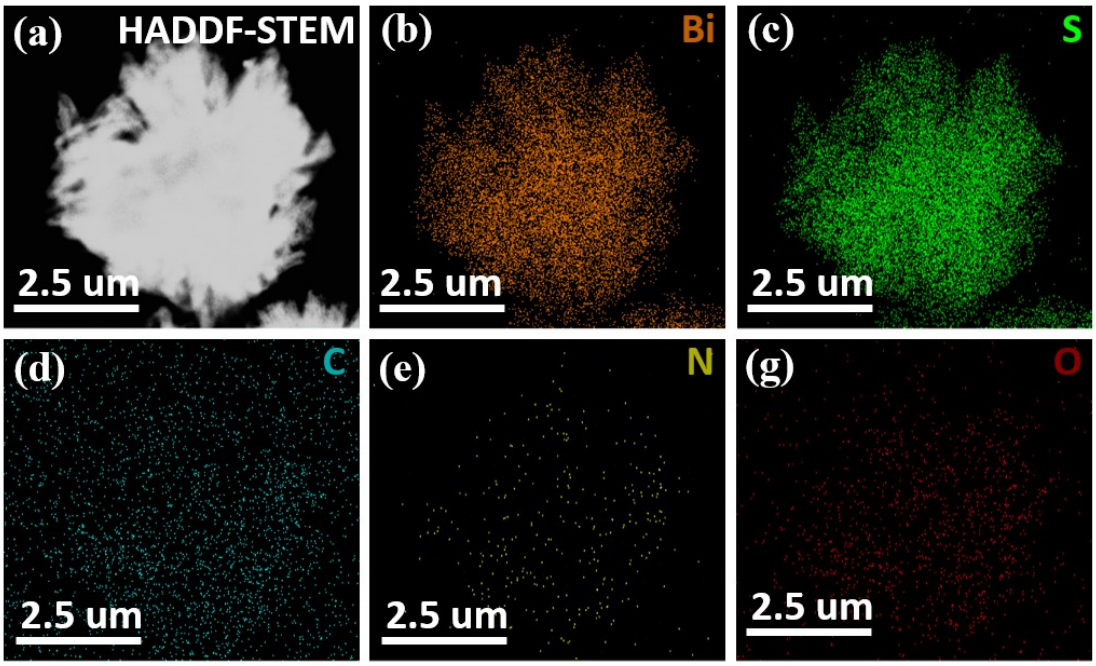

Figure S9. HRTEM images of HAAD-STEM elemental mappings of Bi_2S_3-PPy-1 h.

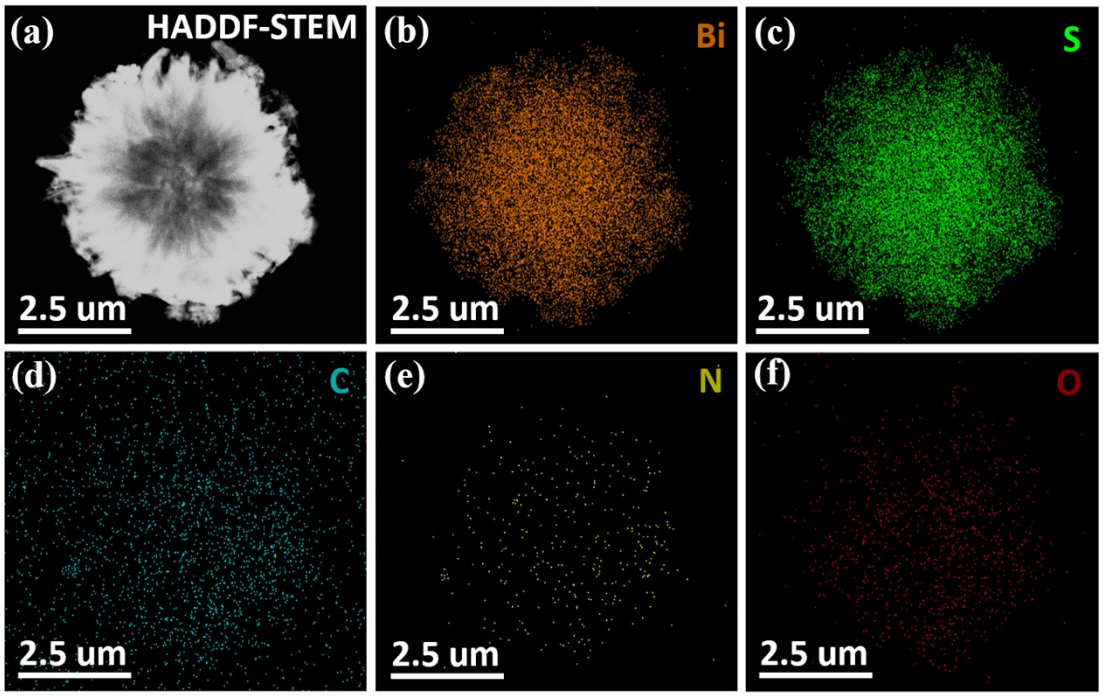

Figure S10. HRTEM images of HAAD-STEM elemental mappings of Bi_2S_3-PPy-5 h.

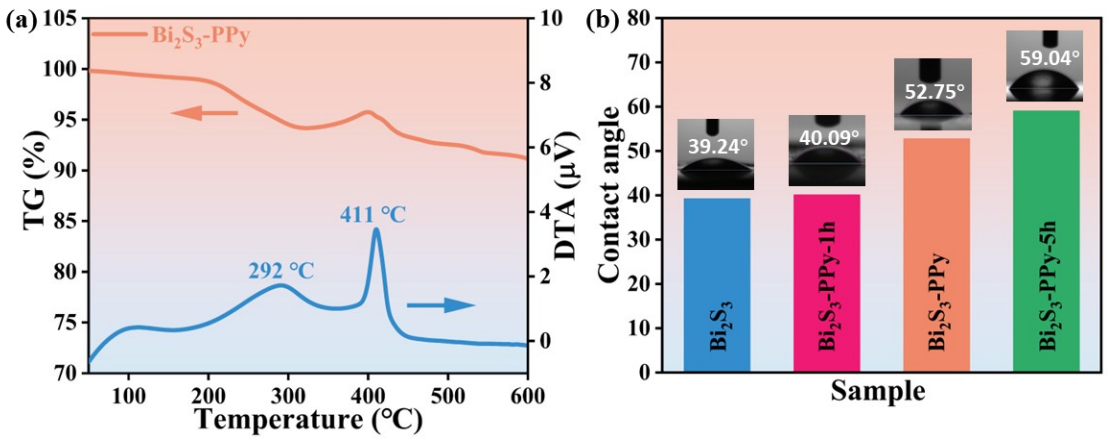

Figure S11. (a) TGA curves of Bi_2S_3-PPy in air. (b) The contact angle measurements of Bi_2S_3, Bi_2S_3-PPy-1 h, Bi_2S_3-PPy, and Bi_2S_3-PPy-5 h.

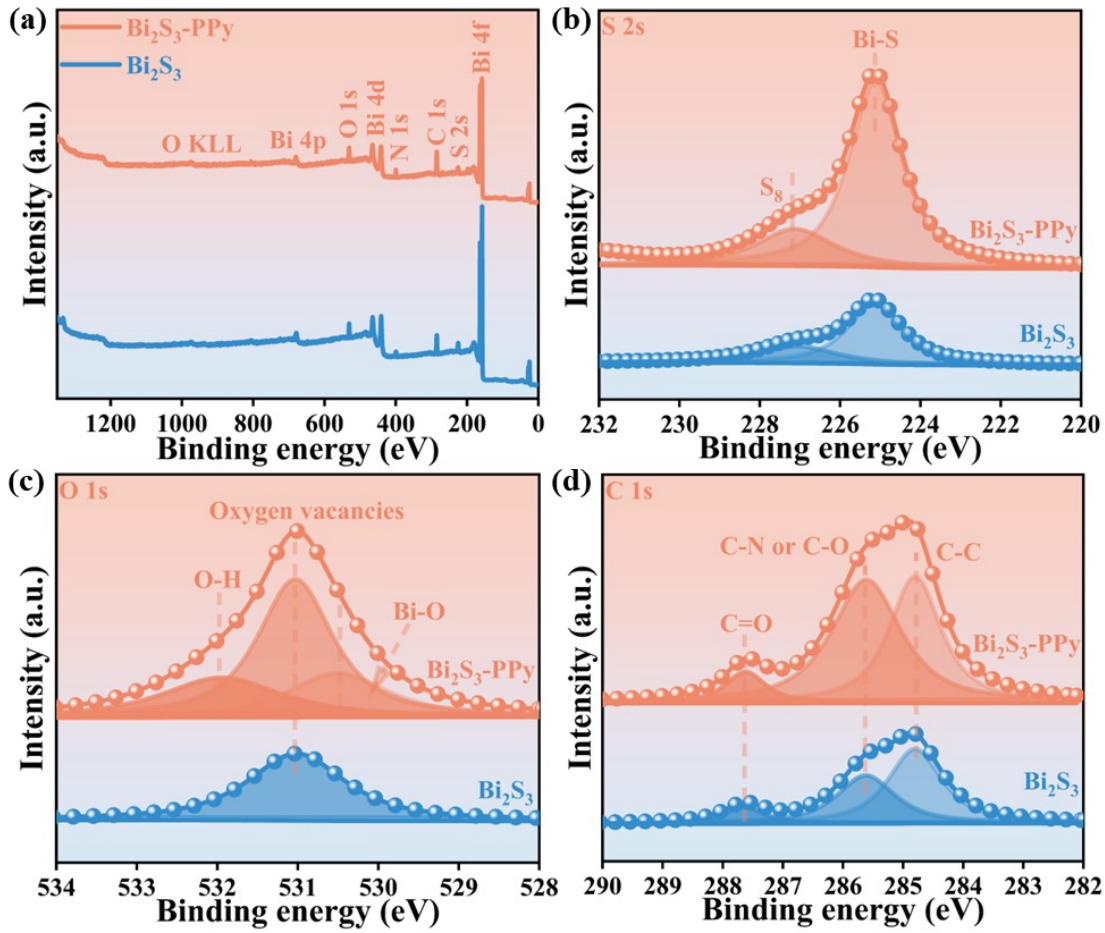

Figure S12. (a) XPS survey spectra, (b) S 2s, (c) O 1s, (d) C 1s XPS spectra of Bi_2S_3 and Bi_2S_3-PPy.

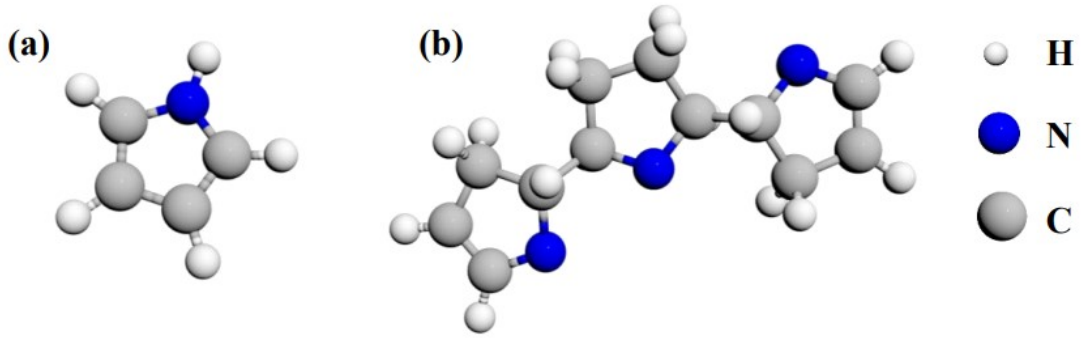

Figure S13. Models of (a) pyrrole and (b) PPy.

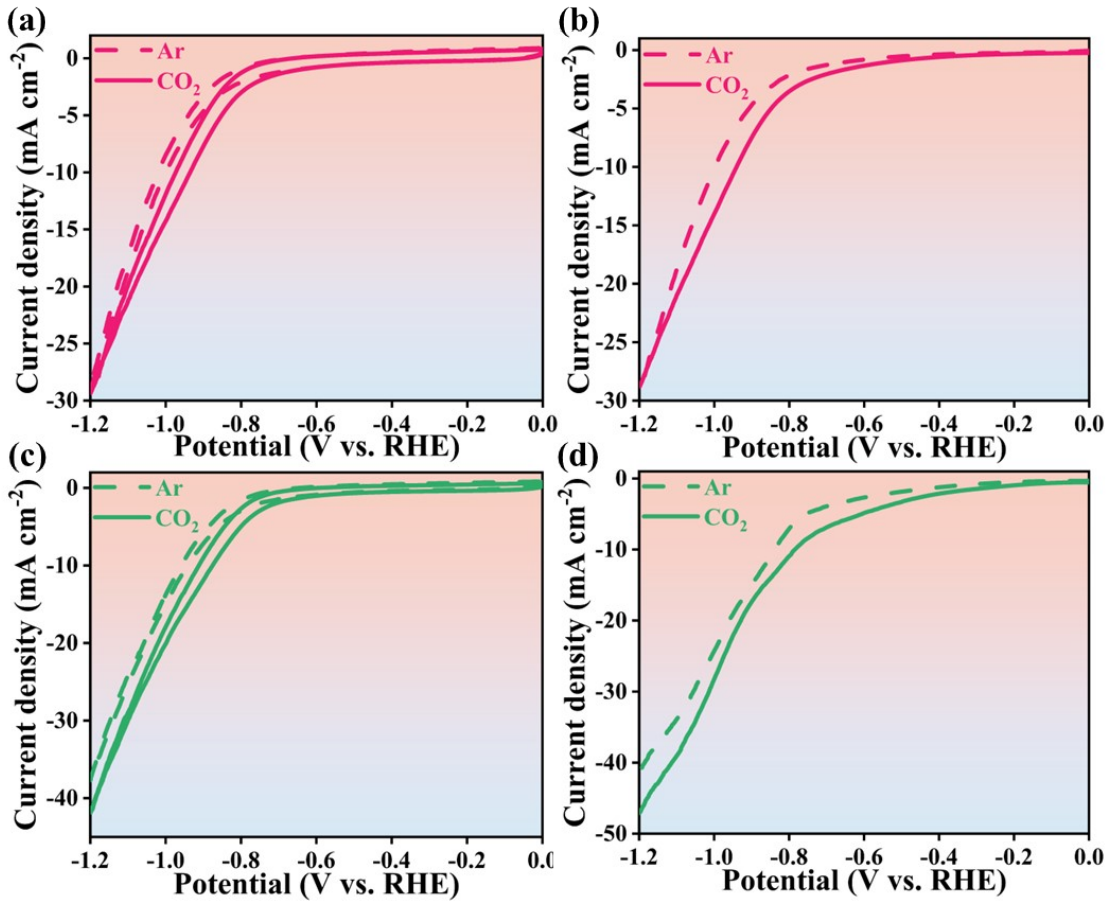

Figure S14. CV curves of (a) Bi_2S_3-PPy-1 h, (c) Bi_2S_3-PPy-5 h in 0.5 M $KHCO_3$ under CO_2 or Ar. LSV plots of (b) Bi_2S_3-PPy-1 h, (d) Bi_2S_3-PPy-5 h in 0.5 M $KHCO_3$ under CO_2 or Ar.

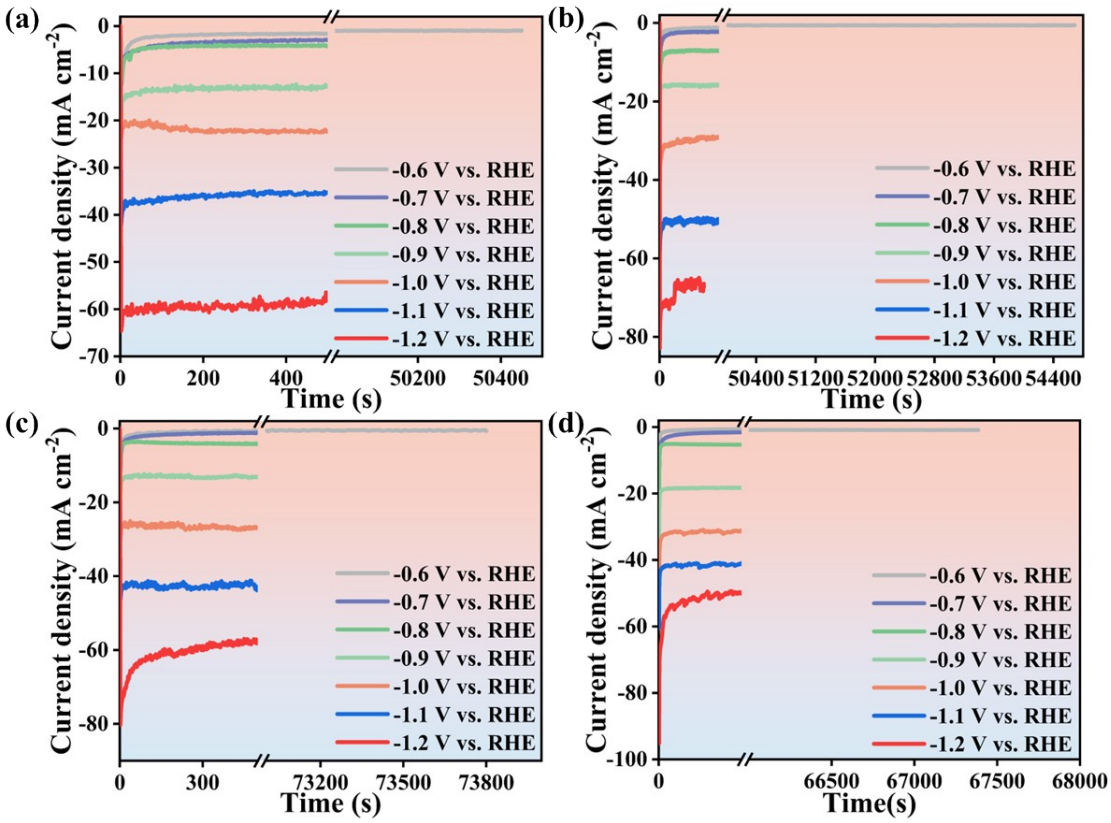

Figure S15. Chronoamperometry curves at various potentials in CO_2-saturated 0.5 M $KHCO_3$ over (a) Bi_2S_3, (b) Bi_2S_3-PPy, (c) Bi_2S_3-PPy-1 h, and (d) Bi_2S_3-PPy-5 h.

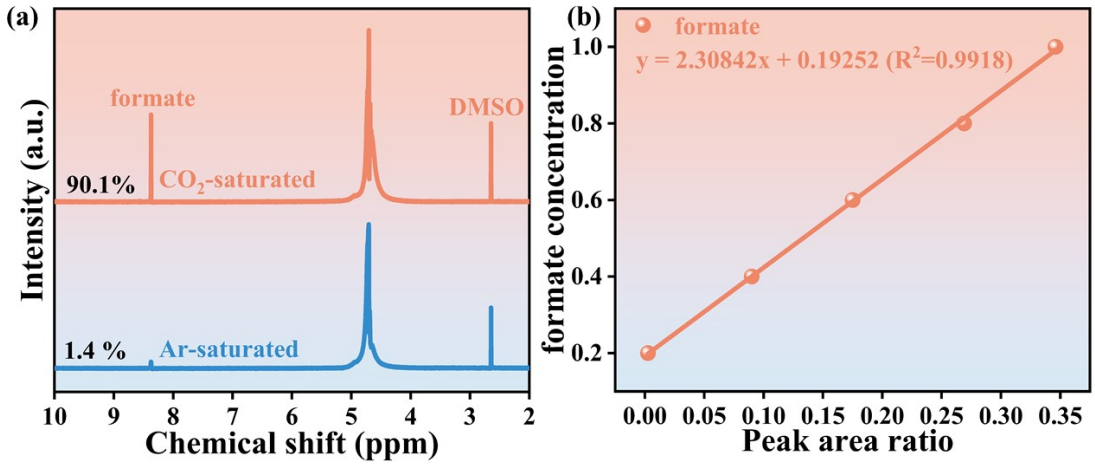

Figure S16. (a) Representative ^{1}H NMR spectra of liquid products in CO_2 or Ar-saturated 0.5 M $KHCO_3$. DMSO is used as an internal standard for the quantification of formate. (b) The calibration curve of formate was calculated from the ^{1}H NMR integral area.

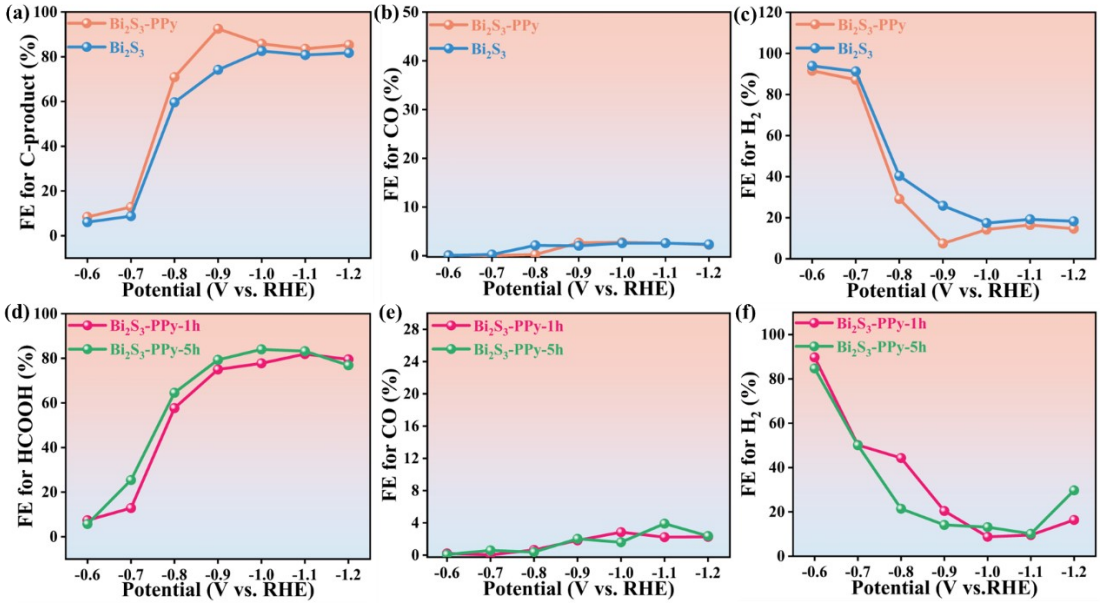

Figure S17. Faradaic efficiency of (a) C-product (CO and formate), (b) CO, and (c) H_2 on Bi_2S_3-PPy and Bi_2S_3. (c) C-product (CO and formate), (d) CO, and (f) H_2 on Bi_2S_3-PPy-1 h and Bi_2S_3-PPy-5 h.

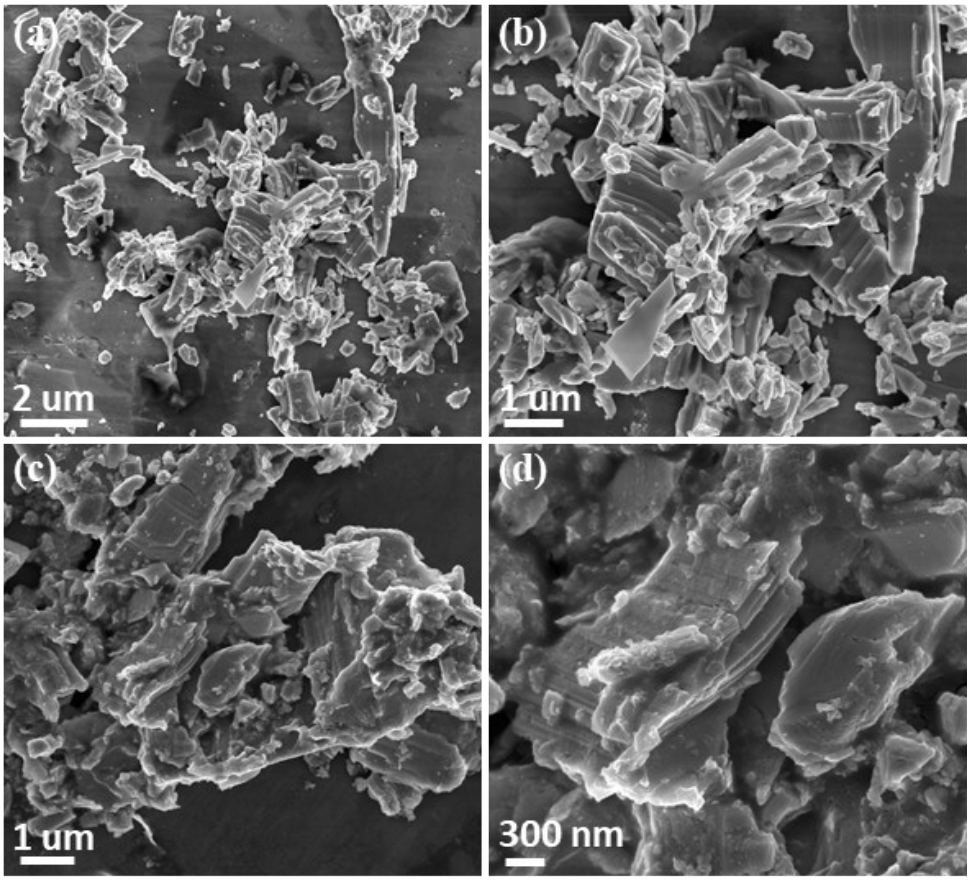

Figure S18. SEM images of (a-b) commercial Bi_2S_3 nanoparticles (com-Bi_2S_3) and commercial Bi_2S_3 coating PPy (com-Bi_2S_3-PPy).

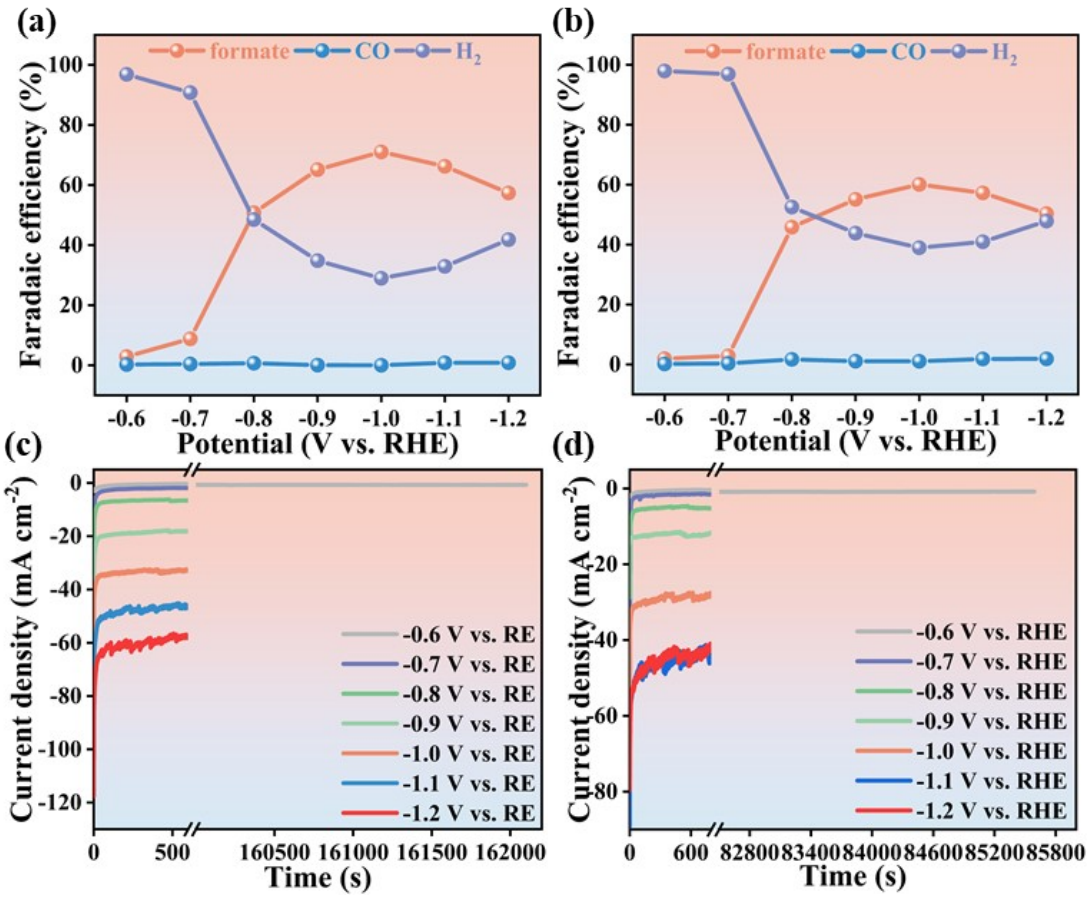

Figure S19. Potential-dependent Faradaic efficiencies of formate、CO and H_2 for (a) Bi_2S_3-PPy without the addition of PVP and (b) com-Bi_2S_3-PPy in CO_2-saturated 0.5 M $KHCO_3$. Potentiostatic curves of (c) Bi_2S_3-PPy without the addition of PVP and (d) com-Bi_2S_3-PPy at various potentials in H-cell.

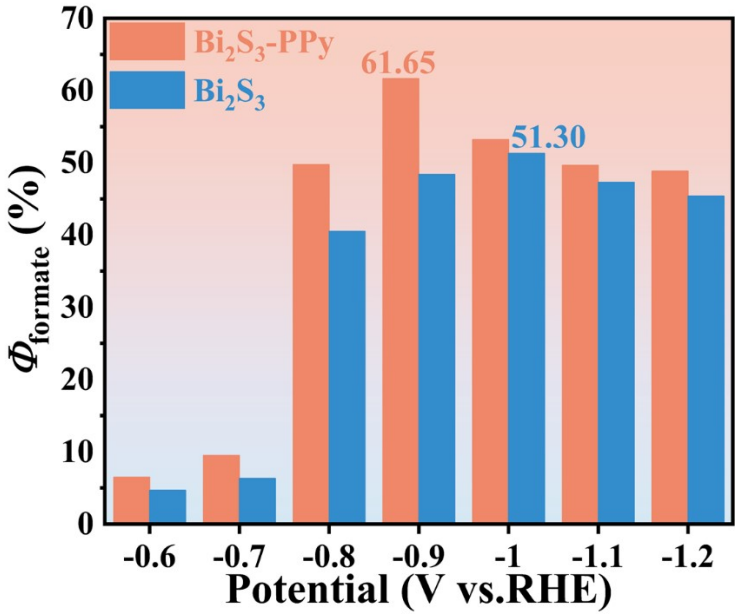

Figure S20. Energy conversion efficiencies for formate production ($\Phi_{formate}$) over Bi_2S_3-PPy and Bi_2S_3.

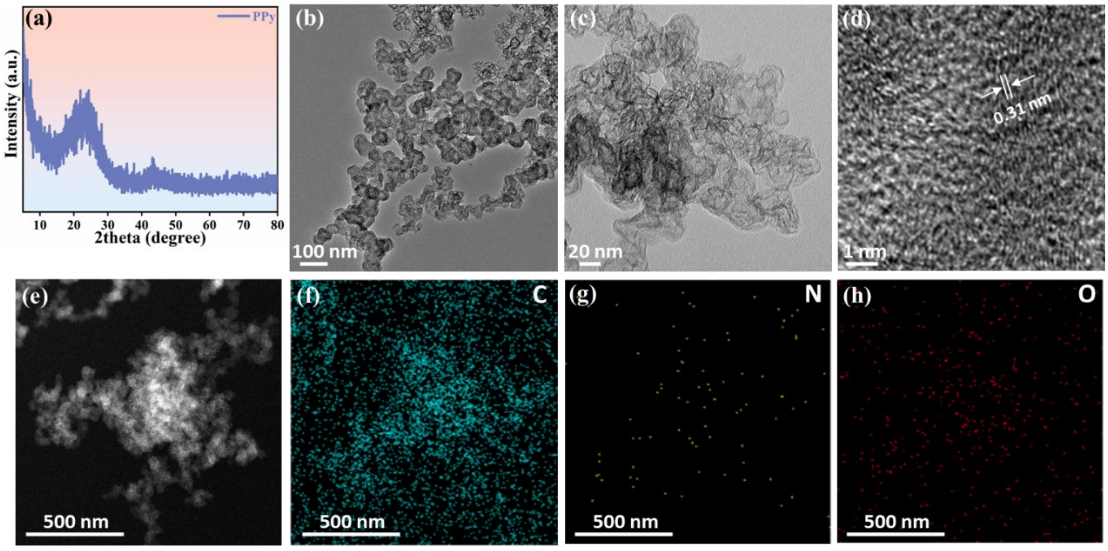

Figure S21. (a) XRD pattern, (b-c) TEM images, (d) HRTEM image, and (e-f) HAAD-STEM elemental mappings of pristine PPy.

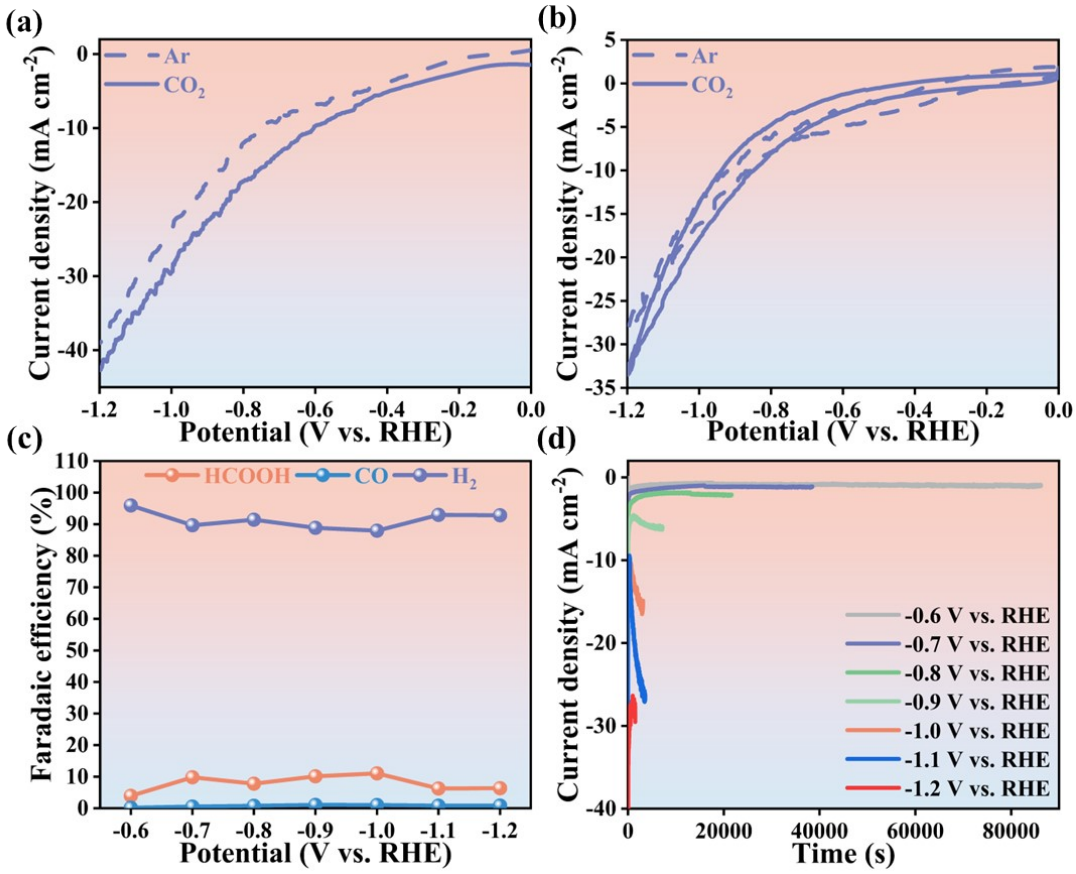

Figure S22. The electrochemical performance of PPy. (a) LSV plots, (b) CV curves in 0.5 M $KHCO_3$ under CO_2 or Ar, (c) FE of reduction products at various potentials, and (d) Chronoamperometry curves at various potentials in CO_2-saturated 0.5 M $KHCO_3$.

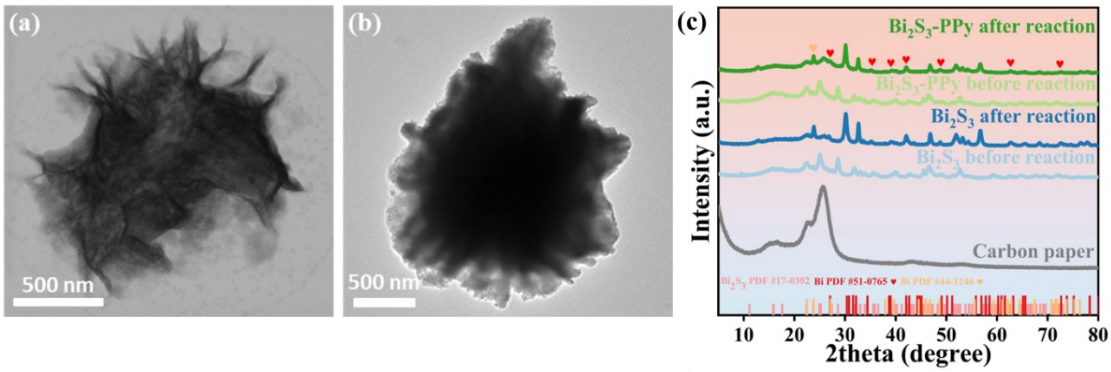

Figure S23. (a-b) TEM images of Bi_2S_3-PPy after CO_2RR measurement. (c) The XRD patterns of Bi_2S_3-PPy and Bi_2S_3 before and after the CO_2RR long-term stability test.

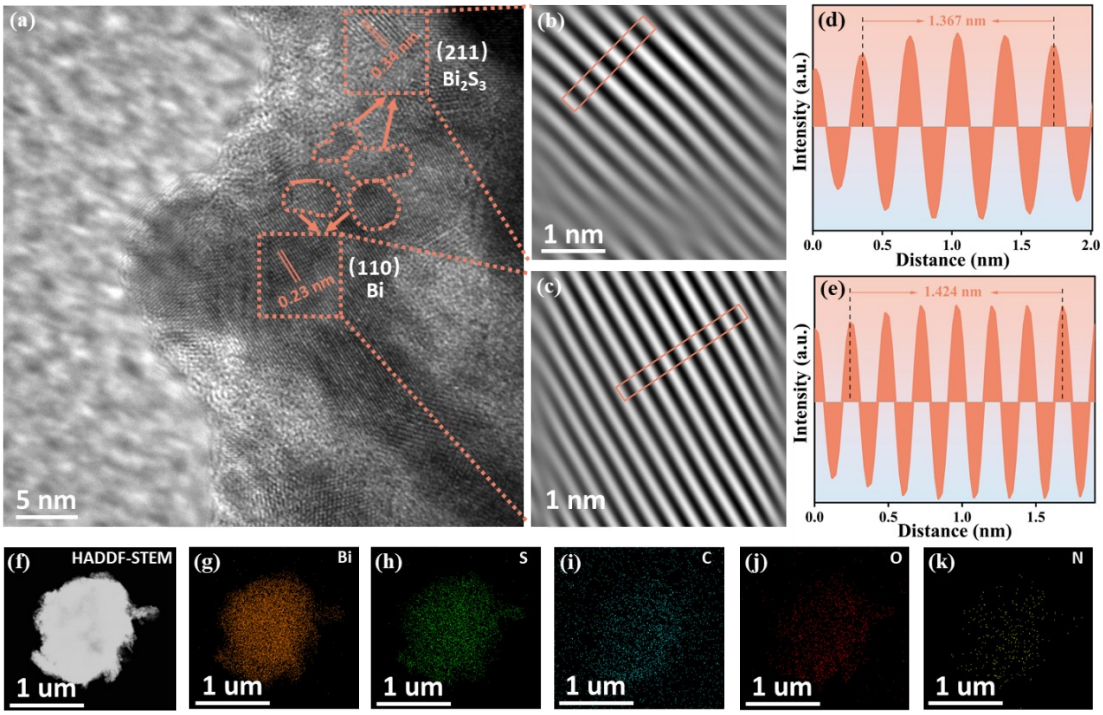

Figure S24. (a-c) HRTEM image, (d-e) Intensity profiles of the lattice fringe corresponding to the orange range. (f) HAADF-STEM image and EDX elemental mappings of Bi_2S_3-PPy composite after CO_2RR long-term stability test.

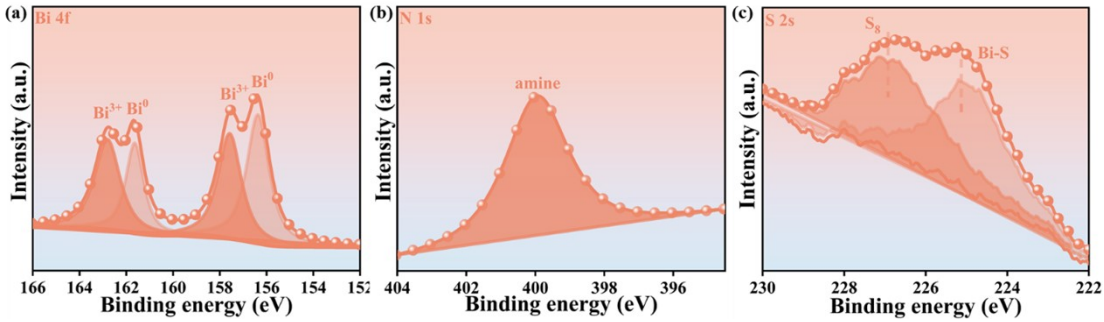

Figure S25. High-resolution (a) Bi 4f, (b) N 1s, (c) S 2s XPS spectra of Bi_2S_3-PPy composite after CO_2RR long-term stability test.

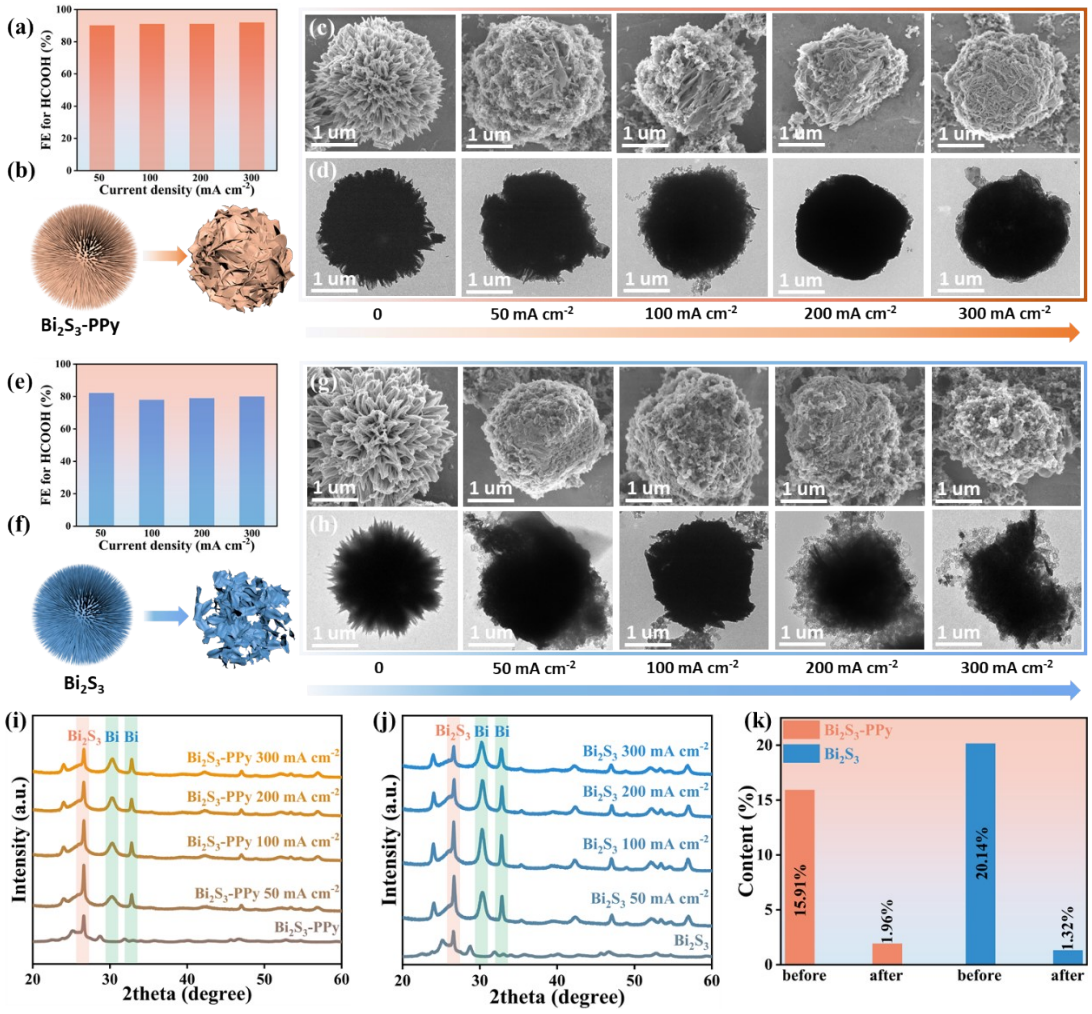

Figure S26. (a, e) FE for formate of Bi_2S_3-PPy and Bi_2S_3 under different current densities, (b, f) schematic illustration of conversion process under large current density, (c, g) SEM images, (d, h) TEM images and (i, j) XRD patterns and (k) the content of S by XPS under a different current density of Bi_2S_3-PPy and Bi_2S_3 before and after CO_2RR under 1 M KOH for 1800 s.

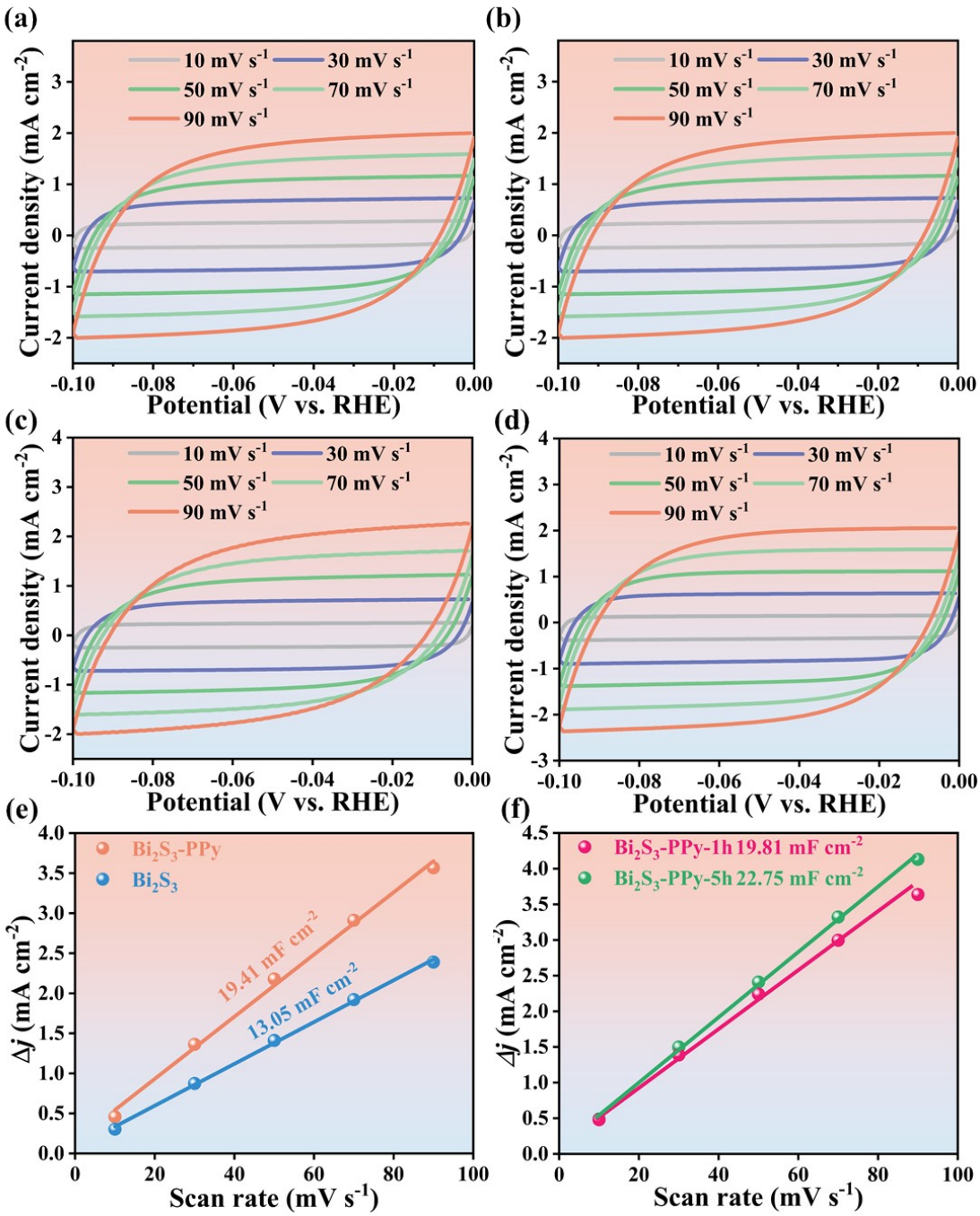

Figure S27. Cyclic voltammograms at the range of -0.1 to 0 V *vs*. RHE with different scan rates (10, 30, 50, 70, 90 mV s^{-1}) for (a) pristine Bi_2S_3, (b) Bi_2S_3-PPy, (c) Bi_2S_3-PPy-1 h, and (d) Bi_2S_3-PPy-5 h. Charging current density differences plotted against scan rates over (e-f) Bi_2S_3, Bi_2S_3-PPy-1 h, Bi_2S_3-PPy, and (f) Bi_2S_3-PPy-5 h.

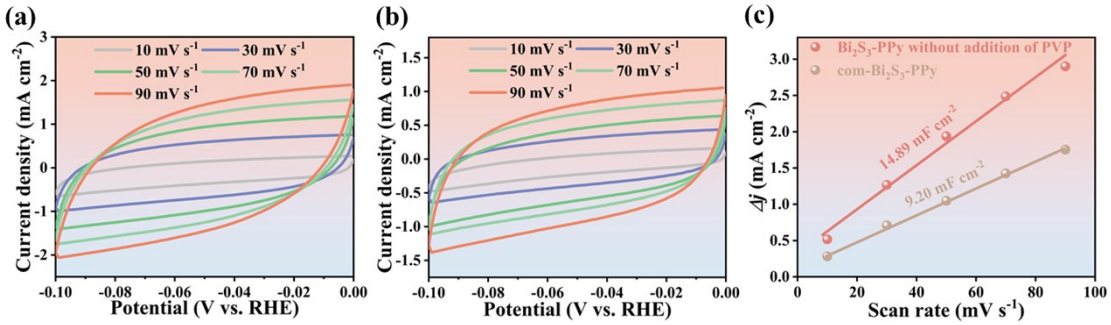

Figure S28. Cyclic voltammograms at the range of -0.1 to 0 V *vs*. RHE with different scan rates (10, 30, 50, 70, 90 mV s^{-1}) for (a) Bi_2S_3-PPy without the addition of PVP, (b) com-Bi_2S_3-PPy. Charging current density differences plotted against scan rates over (c) Bi_2S_3-PPy without the addition of PVP and com-Bi_2S_3-PPy.

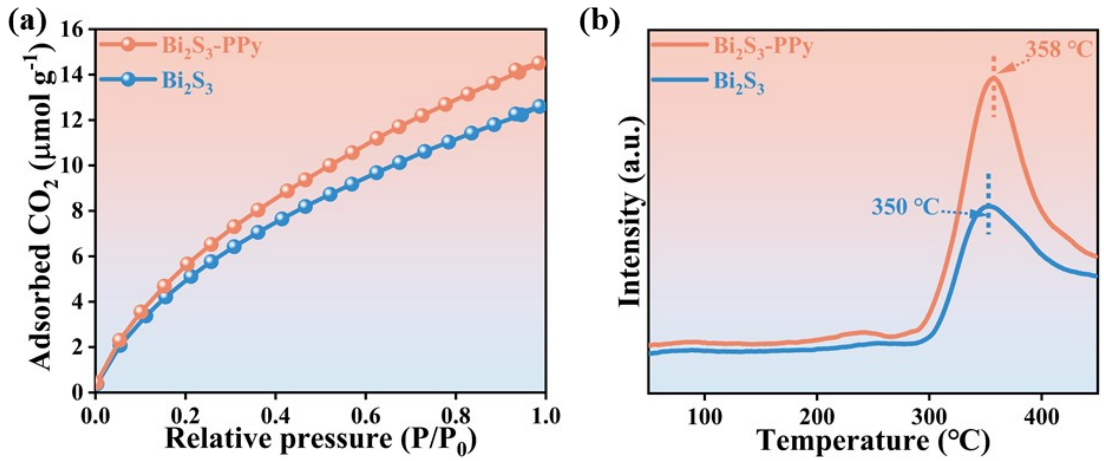

Figure S29. (a) CO_2 adsorption isotherms at 25 ℃, (b) CO_2-TPD spectra of Bi_2S_3 and Bi_2S_3-PPy.

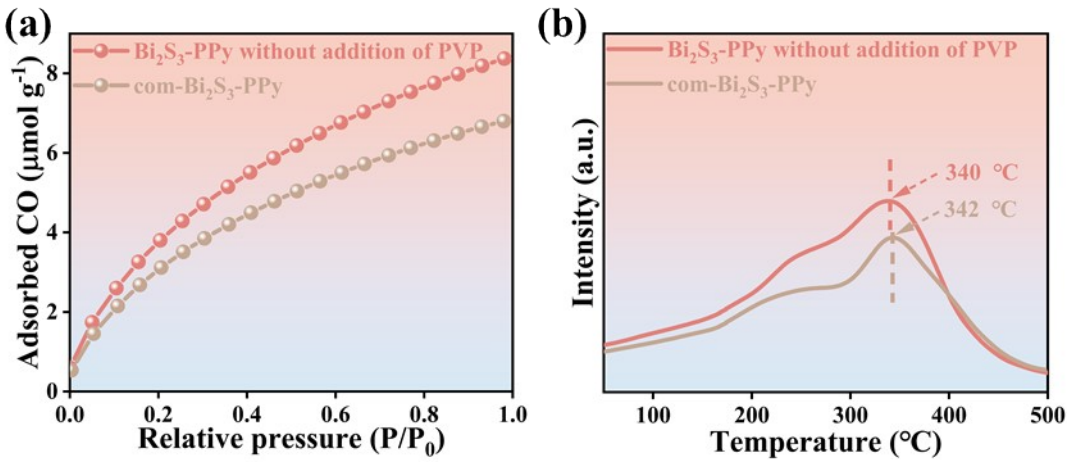

Figure S30. (a) CO_2 adsorption isotherms at 25 ℃, (b) CO_2-TPD spectra of Bi_2S_3-PPy without the addition of PVP and com-Bi_2S_3-PPy.

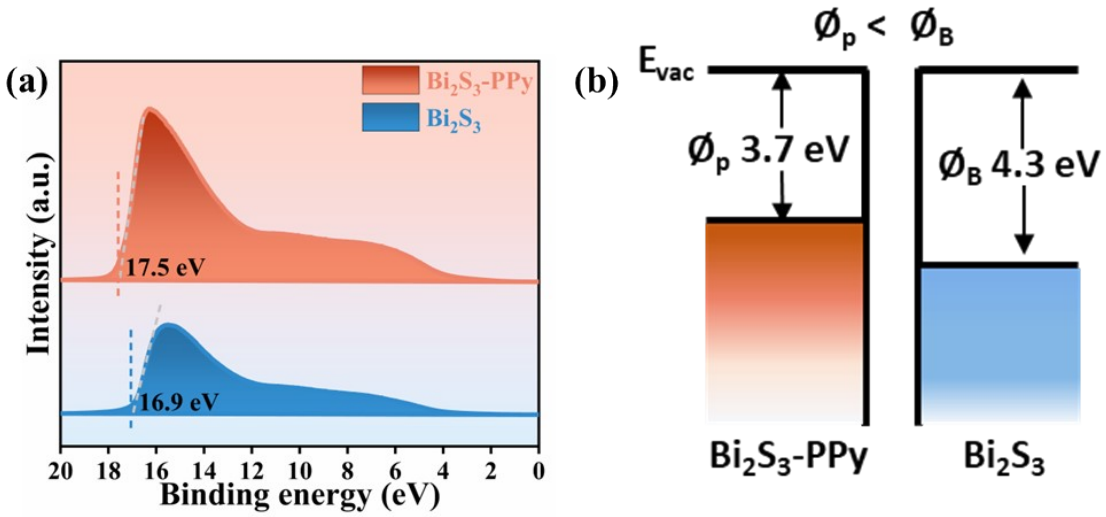

Figure S31. (a) UPS spectra and (b) work function values of Bi_2S_3-PPy and Bi_2S_3.

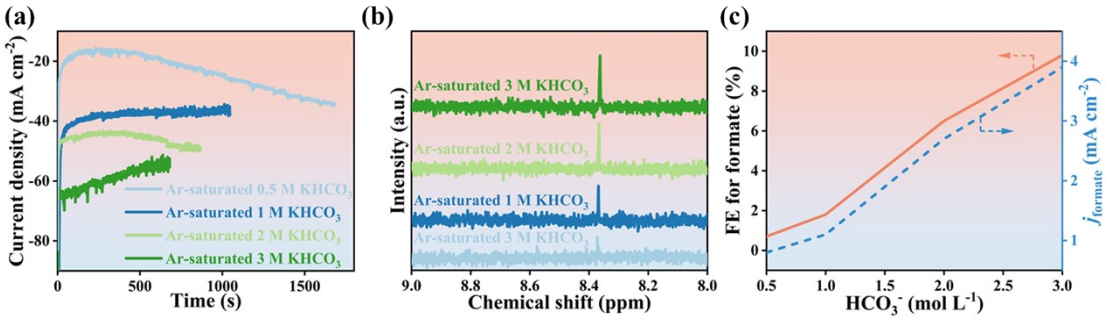

Figure S32. Electrocatalytic performance of Bi_2S_3-PPy in Ar-saturated $KHCO_3$ with different HCO_3^- concentrations: (a) Chronoamperometric responses at the same 20 C; (b) The NMR spectra of the catholyte recycled after electrolysis; (c) $FE_{formate}$ and partial densities of formate.

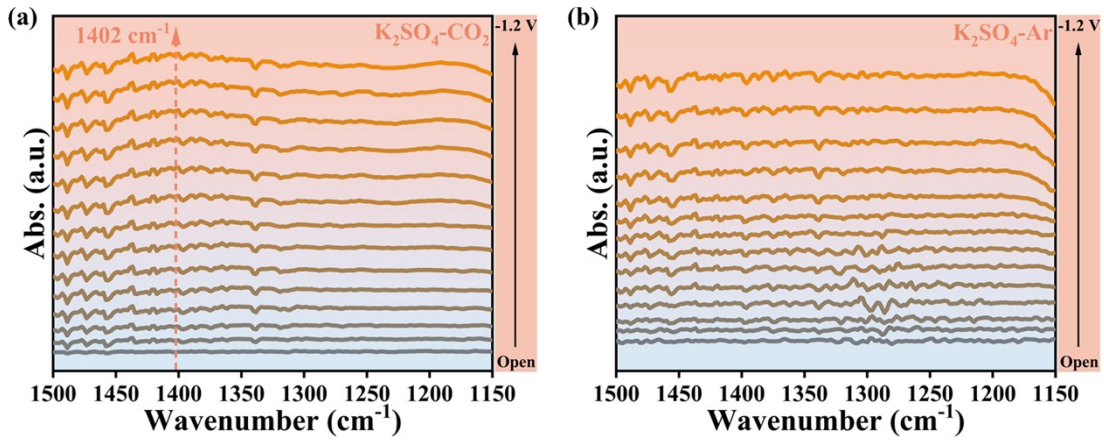

Figure S33. In-situ ATR-IR spectra of Bi_2S_3-PPy collected in (c) CO_2 and (d) Ar-saturated 0.2 M K_2SO_4 under different applied potentials.

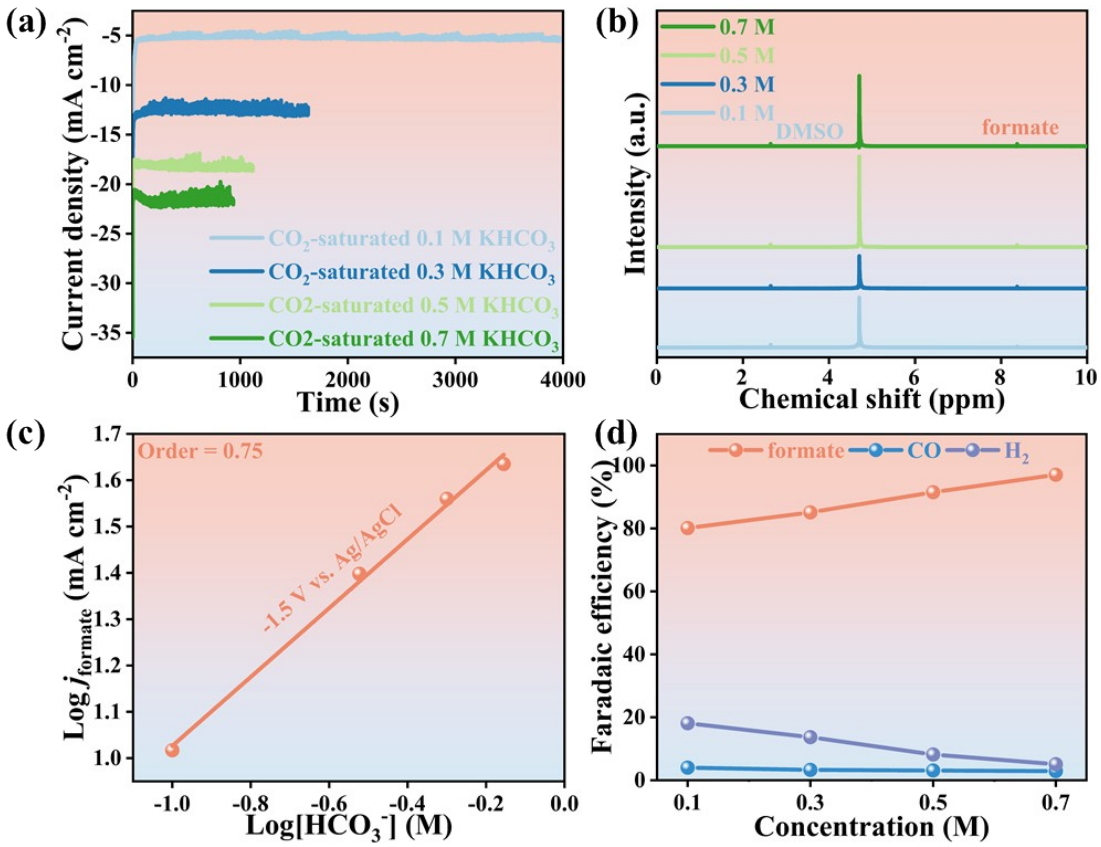

Figure S34. (a) i-t curves, (b) ^{1}H NMR spectra of the electrolyte for Bi_2S_3-PPy with different concentration CO_2-saturated $KHCO_3$ solution. (c) the partial current density of formate plots against the HCO_3^- concentration. (d) Faradaic efficiency of Bi_2S_3-PPy under different concentrations of CO_2-saturated $KHCO_3$.

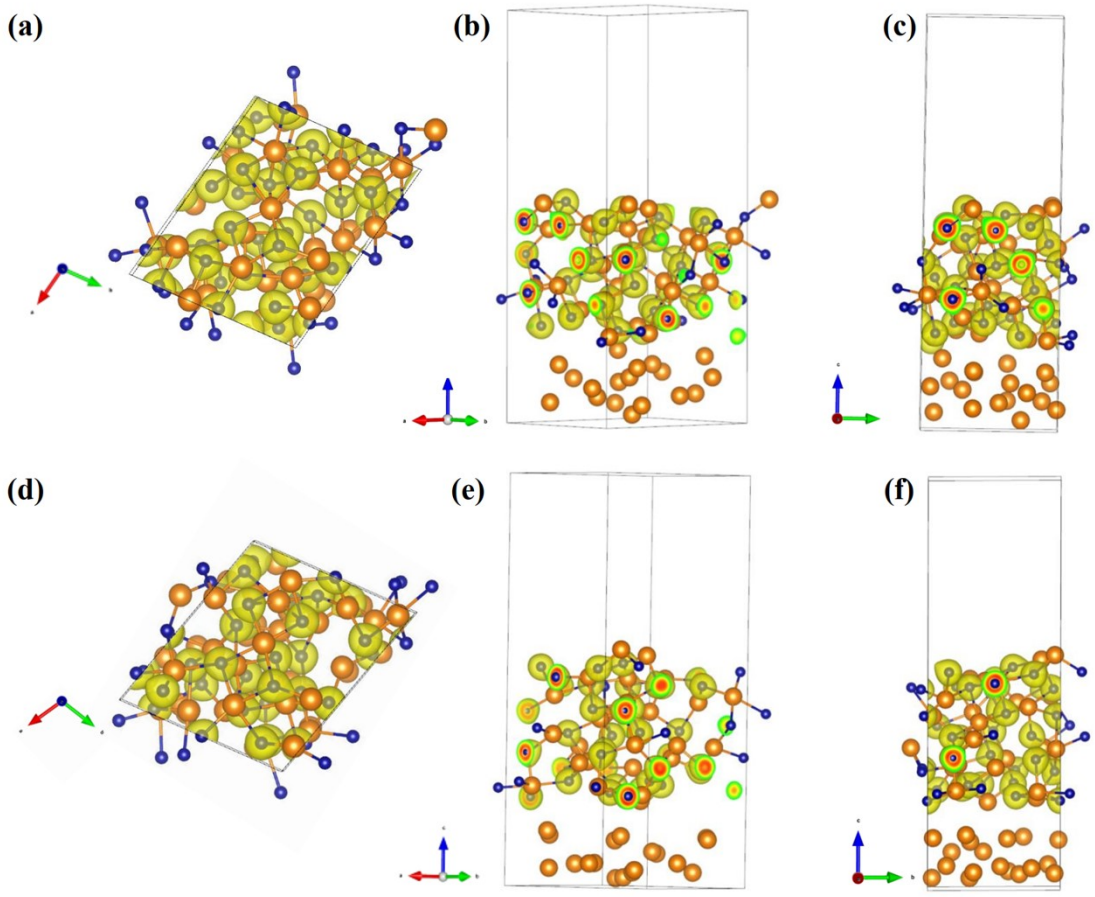

Figure S35. The partial charge density with top view, front view, and side view around the conduction band minimum of (a-c) Bi_2S_3 slab with 2 S vacancies and (d-f) Bi_2S_3-PPy slab with 6 S vacancies, in which yellow refers to charge density contour with the is the value of 0.0001 e/bohr^3. S atoms (blue); Bi atoms (orange).

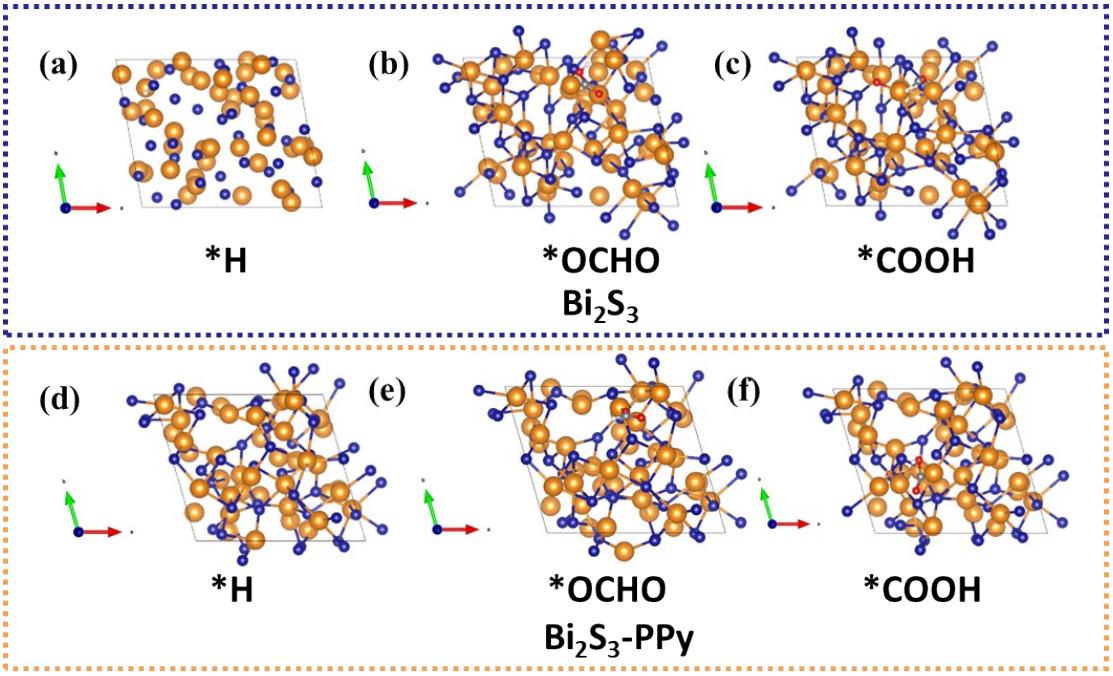

Figure S36. DFT calculation models of (a) *H, (b) *OCHO, and (c) *COOH adsorption on Bi_2S_3 with 2 S vacancies and (d) *H, (e) *OCHO, and (f) *COOH adsorption on Bi_2S_3-PPy with 6 S vacancies. Bi, orange; S, blue; C, grey; O, red; H, white.

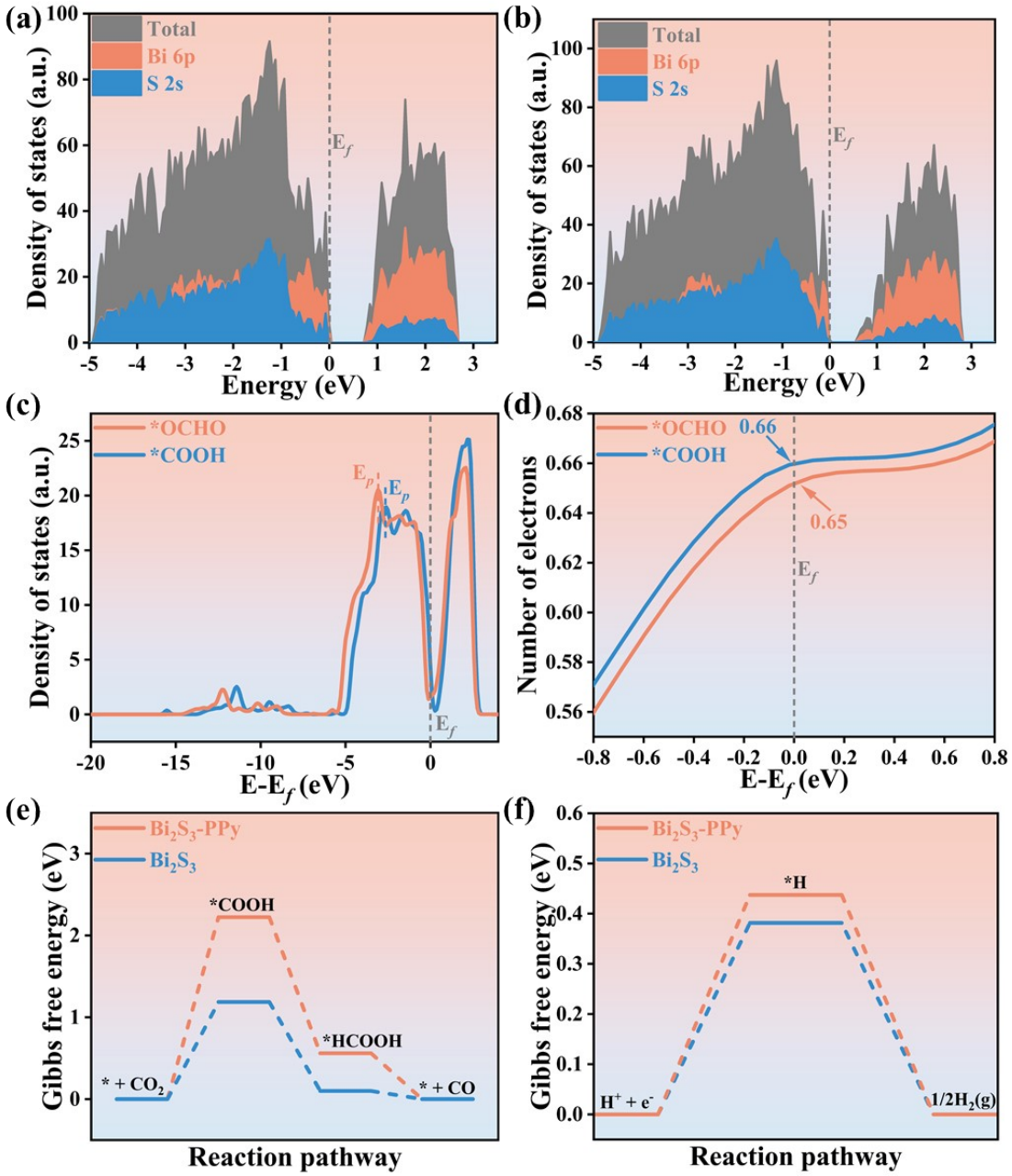

Figure S37. The calculated density of state (DOS) for (a) Bi_2S_3-PPy slab with 6 S vacancies and (b) Bi_2S_3 slab with 2 S vacancies. (c) DOS of the Bi p orbital in Bi_2S_3 with *OCHO and *COOH adsorbed. (d) The corresponding number of electrons in the p orbital per Bi atom with *OCHO and *COOH adsorbed. Calculated reaction energy profiles for (e) CO and (f) H_2 formation on Bi_2S_3 and Bi_2S_3-PPy.

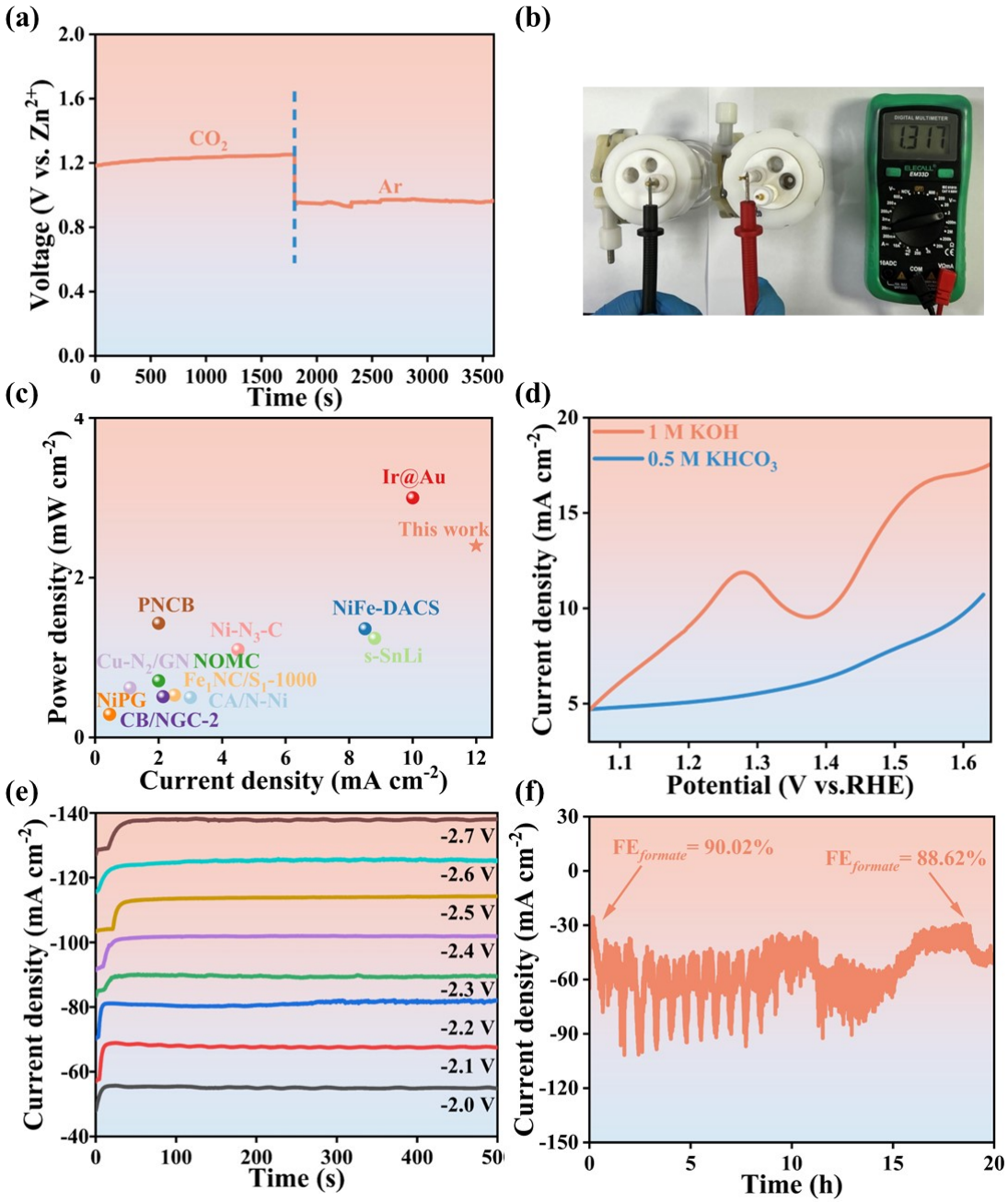

Figure S38. (a) The OCP curve of Bi_2S_3-PPy-based Zn-CO_2 batteries. (b) Digital image of the assembled Zn-CO_2 battery exhibiting a maximum open-circuit voltage of 1.3 V measured using a voltameter. (c) Comparison of power densities towards non-precious metal-based Zn-CO_2 batteries. (d) The LSV curves of commercial RuO_2 in different electrolytes. (e) The i-t curves for combined CO_2RR and OER in an H-Cell configuration. (f) The stability test of Bi_2S_3-PPy for combining CO_2RR and OER.

Table S1. The interaction energy of pyrrole and PPy with sulfide.

Form	Interaction Energy (eV)
Bi_2S_3-Py	-1.125
Bi_2S_3-PPy	-0.530

Table S2. Comparison of the electrocatalytic activity of our catalyst with other state-of-the-art catalysts reported recently for electrochemical reduction of CO_2 to formate in aqueous media.

Electrocatalysts	Overpotential (V)	Formate FE (%)	Formate current density (mA cm^{-2})	References
In_2O_3-rGO	1.00	84.6	22.2	[5]
Ultra Small SnO	0.67	75.0	20.4	[6]
Ag_3Sn NPs	0.80	80.0	15.6	[7]
Sub-2 nm SnO_2 Quantum Wires	0.96	87.3	13.7	[8]
Ag-Bi-S-O Decorated Bi Nanocrystals	0.70	94.3	12.5	[9]
Sn-graphene	0.96	89.0	18.8	[10]
Partially oxidized Co atomic layer	0.16	90.1	9.6	[11]
Bi_2O_3 NSs@MCCM	1.06	93.8	15.2	[12]
BiO_x/C	0.92	93.4	16.1	[13]
Cu foam@BiNW	0.69	95.0	15.0	[14]
Bi_2O_3-NGQDs	0.70	97.6	18.1	[15]
Bi dendrite	0.54	89.0	2.7	[16]
$Bi_2O_2CO_3$ nanosheets	0.70	85.0	9.4	[17]
SnO_2 Nanosheets on carbon cloth	0.88	87.0	45.0	[18]
Sn-pNMs	0.60	80.0	0.8	[19]
Nanostructured	1.07	93.6	9.6	[20]

SnO_2				
Sn-CF 1000	0.60	63.0	11.0	[21]
Dendritic $Cu_{0.2}In_{0.8}$	0.6	62.0	0.7	[22]
PEI-NCNT	1.07	87.0	8.3	[23]
Bi_2S_3-PPy	**0.9**	**91.18**	**15**	**This work**

Table S3. Comparison of the electrocatalytic activity of our catalyst with other state-of-the-art catalysts reported recently for electrochemical reduction of CO_2 to formate in aqueous media.

Electrocatalysts	Overpotential (V)	Formate FE (%)	Formate current density (mA cm^{-2})	References
Bi@Sn	-	92.2	-230.5	[24]
Bi_2O_3 NT	0.58	95	-119.5	[25]
N-Sn(S)	0.80	93.3	-21	[26]
SnO_2 NP	1.21	92.8	-64	[27]
Bi-ene	-	99.6	-100	[28]
BiOBr	-	90	-180	[29]
Bi-NSs	1.51	86.9	-373	[30]
S-$BiVO_4$	1.00	97.4	-105.4	[31]
$ZnIn_2S_4$	-	99.3	-297.8	[32]
Bi_2S_3-Bi_2O_3	-	90	-200	[33]
PD-Bi	-	90.7	-200	[34]
Pb_1Cu	-	92	-1000	[35]
s-LiSn	-	94	-1000	[36]
AI5S8	-	94	-560	[37]
BOC	-	87	-230	[38]
Bi NRs	-	95	-200	[39]
Bi-NBs	-	95	-330	[40]
Bi_2S_3-PPy	**0.78**	**98%**	**-250**	**This work**
	0.98	**92%**	**-300**	**This work**

Table S4. Free energy of *OCHO, *COOH, *CO, *H absorption, and E_p on various DFT models.

Free energy (eV)	Bi_2S_3	Bi_2S_3-PPy
*OCHO	0.534	0.1777
*COOH	1.186	2.223
*CO	0.1	0.56
*H	0.3815	0.4373
E_p	-3.07	-0.81

Table S5. The performance comparison of Zn-CO_2 batteries.

Catalysts	FE_{CO}	Power density (mW cm^{-2})	Current density (mA cm^{-2})	Reference
CA/N-Ni	98	0.5	3	[41]
NiFe-DASC	90.6	1.36	8.5	[42]
s-SnLi	-	1.24	8.8	[43]
NOMC	76	0.71	2	[44]
Ni-N_3-C	93	1.1	4.5	[45]
Ir@Au	90	3	10	[46]
Fe_1NC/S_1-1000	-	0.53	2.5	[47]
NiPG	66	0.29	0.46	[48]
Cu-N_2/GN	64	0.62	1.1	[49]
CB-NGC-2	80.4	0.51	2.14	[50]
PNCB	11 (formate)	1.43	2	[51]
Bi_2S_3-PPy	**93 (formate)**	**2.4**	**12**	**This work**

Table S6. The property comparison towards various catalysts for CO_2-OER electrolysis.

Cathode	Catholyte	Anode	Anolyte	Voltage (V) at 10 mA cm^{-2}	Reference
SiNC	1 M KCO_3	SiNC	1 M KOH	>2.5	[52]
CoPc-CNT	2 M $KHCO_3$	NiFe-HC	2 M $KHCO_3$	~2.21	[53]
Co_2FeO_4	0.5 M $KHCO_3$	Co_2FeO_4	1.0 M KOH	~2.25	[54]
Mp-SnO_2	0.5 M $NaHCO_3$	IrO_2	0.5 M $NaHCO_3$	>3	[55]
Bi(B)-2	0.5 M $KHCO_3$	FeP NS/NF	0.5 M $KHCO_3$	~2.48	[56]
Bi-ene	0.5 M $KHCO_3$	RuO_2	1.0 M KOH	2.38	[57]
Bi_2O_3	0.5 M $KHCO_3$	Pt wire	1.0 M KOH	>3	[58]
BiNS	0.5 M $NaHCO_3$	Ir/C	0.5 M $NaHCO_3$	3.2	[59]
PNCB	0.5 M $KHCO_3$	Ir/C	0.5 M $NaHCO_3$	2.71	[51]
Bi_2S_3-PPy	**0.5 M $KHCO_3$**	**RuO_2**	**0.5 M $KHCO_3$**	**2.18**	**This work**
Bi_2S_3-PPy	**0.5 M $KHCO_3$**	**RuO_2**	**1.0 M KOH**	**2.05**	**This work**

References

1. G. Kresse and D. Joubert, *Phys. Rev. B*, 1999, **59**, 1758-1775.
2. J. P. Perdew, K. Burke and M. Ernzerhof, *Phys. Rev. Lett.*, 1996, **77**, 3865-3868.
3. S. Grimme, J. Antony, S. Ehrlich and H. Krieg, *J. Chem. Phys.* 2010, **132**, 154104.
4. C.-C. He, J.-H. Liao, S.-B. Qiu, Y.-J. Zhao and X.-B. Yang, *Comput. Mater. Sci.*, 2021, **193**, 110386.
5. Z. Zhang, F. Ahmad, W. Zhao, W. Yan, W. Zhang, H. Huang, C. Ma and J. Zeng, *Nano Lett.*, 2019, **19**, 4029-4034.
6. J. Gu, F. Héroguel, J. Luterbacher and X. Hu, *Science*, 2018, **57**, 2943-2947.
7. W. Luc, C. Collins, S. Wang, H. Xin, K. He, Y. Kang and F. Jiao, *J. Am. Chem. Soc.*, 2017, **139**, 1885-1893.
8. S. Liu, J. Xiao, X. F. Lu, J. Wang, X. Wang and X. W. Lou, *Angew. Chem., Int. Ed.*, 2019, **58**, 8499-8503.
9. J.-H. Zhou, K. Yuan, L. Zhou, Y. Guo, M.-Y. Luo, X.-Y. Guo, Q.-Y. Meng and Y.-W. Zhang, *Angew. Chem., Int. Ed.*, 2019, **58**, 14197-14201.
10. F. Lei, W. Liu, Y. Sun, J. Xu, K. Liu, L. Liang, T. Yao, B. Pan, S. Wei and Y. Xie, *Nat. Commun.*, 2016, **7**, 12697.
11. S. Gao, Y. Lin, X. Jiao, Y. Sun, Q. Luo, W. Zhang, D. Li, J. Yang and Y. Xie, *Nature*, 2016, **529**, 68-71.
12. S. Liu, X. F. Lu, J. Xiao, X. Wang and X. W. D. Lou, *Angew. Chem., Int. Ed.*, 2019, **58**, 13828-13833.
13. C. W. Lee, J. S. Hong, K. D. Yang, K. Jin, J. H. Lee, H.-Y. Ahn, H. Seo, N.-E. Sung and K. T. Nam, *ACS Cataly.*, 2018, **8**, 931-937.
14. X. Zhang, X. Sun, S.-X. Guo, A. M. Bond and J. Zhang, *Energy Environ. Sci.*, 2019, **12**, 1334-1340.
15. Z. Chen, K. Mou, X. Wang and L. Liu, *C, Angew. Chem., Int. Ed.*, 2018, **57**, 12790-12794.
16. J. H. Koh, D. H. Won, T. Eom, N.-K. Kim, K. D. Jung, H. Kim, Y. J. Hwang and B. K. Min, *ACS Cataly.*, 2017, **7**, 5071-5077.
17. Y. Zhang, X. Zhang, Y. Ling, F. Li, A. M. Bond and J. Zhang, *Energy Environ. Sci.*, 2018, **57**, 13283-13287.
18. F. Li, L. Chen, G. P. Knowles, D. R. MacFarlane and J. Zhang, *Angew. Chem., Int. Ed.*, 2017, **56**, 505-509.
19. B. Kumar, V. Atla, J. P. Brian, S. Kumari, T. Q. Nguyen, M. Sunkara and J. M. Spurgeon, *Angew. Chem., Int. Ed.*, 2017, **56**, 3645-3649.
20. S. Zhang, P. Kang and T. J. Meyer, *J. Am. Chem. Soc.*, 2014, **136**, 1734-1737.
21. Y. Zhao, J. Liang, C. Wang, J. Ma and G. G. Wallace, *Adv. Energy Mater.*, 2018, **8**, 1702524.
22. Z. B. Hoffman, T. S. Gray, K. B. Moraveck, T. B. Gunnoe and G. Zangari, *ACS Cataly.*, 2017, **7**, 5381-5390.
23. S. Zhang, P. Kang, S. Ubnoske, M. K. Brennaman, N. Song, R. L. House, J. T. Glass and T. J. Meyer, *J. Am. Chem. Soc.*, 2014, **136**, 7845-7848.

24. Y. Xing, X. Kong, X. Guo, Y. Liu, Q. Li, Y. Zhang, Y. Sheng, X. Yang, Z. Geng and J. Zeng, *Adv. Sci.*, 2020, **7**, 1902989.
25. Q. Gong, P. Ding, M. Xu, X. Zhu, M. Wang, J. Deng, Q. Ma, N. Han, Y. Zhu, J. Lu, Z. Feng, Y. Li, W. Zhou and Y. Li, *Nat. Commun.*, 2019, **10**, 2807.
26. H. Cheng, S. Liu, J. Zhang, T. Zhou, N. Zhang, X.-s. Zheng, W. Chu, Z. Hu, C. Wu and Y. Xie, *Nano Lett.*, 2020, **20**, 6097-6103.
27. C. Liang, B. Kim, S. Yang, L. Yang, C. Francisco Woellner, Z. Li, R. Vajtai, W. Yang, J. Wu, P. J. A. Kenis and Pulickel M. Ajayan, *J. Mater. Chem. A*, 2018, **6**, 10313-10319.
28. C. Cao, D.-D. Ma, J.-F. Gu, X. Xie, G. Zeng, X. Li, S.-G. Han, Q.-L. Zhu, X.-T. Wu and Q. Xu, *Angew. Chem., Int. Ed.*, 2020, **59**, 15014-15020.
29. F. P. García de Arquer, O. S. Bushuyev, P. De Luna, C.-T. Dinh, A. Seifitokaldani, M. I. Saidaminov, C.-S. Tan, L. N. Quan, A. Proppe, M. G. Kibria, S. O. Kelley, D. Sinton and E. H. Sargent, *Adv. Mater.*, 2018, **30**, 1802858.
30. J. Yang, X. Wang, Y. Qu, X. Wang, H. Huo, Q. Fan, J. Wang, L.-M. Yang and Y. Wu, *Adv. Energy Mater.*, 2020, **10**, 2001709.
31. W. Ma, J. Bu, Z. Liu, C. Yan, Y. Yao, N. Chang, H. Zhang, T. Wang and J. Zhang, *Adv. Funct. Mater.*, 2021, **31**, 2006704.
32. L.-P. Chi, Z.-Z. Niu, X.-L. Zhang, P.-P. Yang, J. Liao, F.-Y. Gao, Z.-Z. Wu, K.-B. Tang and M.-R. Gao, *Nat. Commun.*, 2021, **12**, 5835.
33. P. F. Sui, C. Xu, M. N. Zhu, S. Liu, Q. Liu and J. L. Luo, *Small*, 2022, **18**, e2105682.
34. Y. Wang, Y. Li, J. Liu, C. Dong, C. Xiao, L. Cheng, H. Jiang, H. Jiang and C. Li, *Angew. Chem., Int. Ed.*, 2021, **60**, 7681-7685.
35. T. Zheng, C. Liu, C. Guo, M. Zhang, X. Li, Q. Jiang, W. Xue, H. Li, A. Li, C.-W. Pao, J. Xiao, C. Xia and J. Zeng, *Nat. Nanotechnol.*, 2021, **16**, 1386-1393.
36. S. Yan, C. Peng, C. Yang, Y. Chen, J. Zhang, A. Guan, X. Lv, H. Wang, Z. Wang, T.-K. Sham, Q. Han and G. Zheng, *Angew. Chem., Int. Ed.*, 2021, **60**, 25741-25745.
37. J. Zhang, T. Fan, P. Huang, X. Lian, Y. Guo, Z. Chen and X. Yi, *Adv. Funct. Mater.*, 2022, **32**, 2113075.
38. P. F. Sui, M. R. Gao, S. Liu, C. Xu, M. N. Zhu and J. L. Luo, *Adv. Funct. Mater.*, 2022, **32**, 2203647.
39. Y. Li, J. Chen, S. Chen, X. Liao, T. Zhao, F. Cheng and H. Wang, *ACS Energy Lett.*, 2022, **7**, 1454-1461.
40. G. Zeng, Y. He, D.-D. Ma, S. Luo, S. Zhou, C. Cao, X. Li, X.-T. Wu, H.-G. Liao and Q.-L. Zhu, *Adv. Funct. Mater.*, 2022, **32**, 2201125.
41. Y. Zhang, X. Wang, S. Zheng, B. Yang, Z. Li, J. Lu, Q. Zhang, N. M. Adli, L. Lei, G. Wu and Y. Hou, *Adv. Funct. Mater.*, 2021, **31**, 2104377.
42. Z. Zeng, L. Y. Gan, H. Bin Yang, X. Su, J. Gao, W. Liu, H. Matsumoto, J. Gong, J. Zhang, W. Cai, Z. Zhang, Y. Yan, B. Liu and P. Chen, *Nat. Commun.*, 2021, **12**, 4088.
43. S. Yan, C. Peng, C. Yang, Y. Chen, J. Zhang, A. Guan, X. Lv, H. Wang, Z. Wang, T.-K. Sham, Q. Han and G. Zheng, *Angew. Chem., Int. Ed.*, 2021, **60**, 25741-25745.
44. S. Gao, Y. Liu, Z. Xie, Y. Qiu, L. Zhuo, Y. Qin, J. Ren, S. Zhang, G. Hu, J. Luo and X. Liu, *Small Methods*, 2021, **5**, 2001039.
45. Y. Zhang, L. Jiao, W. Yang, C. Xie and H.-L. Jiang, *Angew. Chem., Int. Ed.*, 2021, **60**, 7607-7611.

46. X. Wang, J. Xie, M. A. Ghausi, J. Lv, Y. Huang, M. Wu, Y. Wang and J. Yao, *Adv. Mater.*, 2019, **31**, 1807807.
47. T. Wang, X. Sang, W. Zheng, B. Yang, S. Yao, C. Lei, Z. Li, Q. He, J. Lu, L. Lei, L. Dai and Y. Hou, *Adv. Mater.,* 2020, **32**, 2002430.
48. R. Yang, J. Xie, Q. Liu, Y. Huang, J. Lv, M. A. Ghausi, X. Wang, Z. Peng, M. Wu and Y. Wang, *J. Mater. Chem. A*, 2019, **7**, 2575-2580.
49. W. Zheng, J. Yang, H. Chen, Y. Hou, Q. Wang, M. Gu, F. He, Y. Xia, Z. Xia, Z. Li, B. Yang, L. Lei, C. Yuan, Q. He, M. Qiu and X. Feng, *Adv. Funct. Mater.*, 2020, **30**, 1907658.
50. X. Hao, X. An, A. M. Patil, P. Wang, X. Ma, X. Du, X. Hao, A. Abudula and G. Guan, *ACS Appl. Mater. Interfaces*, 2021, **13**, 3738-3747.
51. Y. Wang, L. Xu, L. Zhan, P. Yang, S. Tang, M. Liu, X. Zhao, Y. Xiong, Z. Chen and Y. Lei, *Nano Energy*, 2022, **92**, 106780.
52. M. A. Ghausi, J. Xie, Q. Li, X. Wang, R. Yang, M. Wu, Y. Wang and L. Dai, *Angew. Chem., Int. Ed.*, 2018, **57**, 13135-13139.
53. Y. Meng, X. Zhang, W.-H. Hung, J. He, Y.-S. Tsai, Y. Kuang, M. J. Kenney, J.-J. Shyue, Y. Liu, K. H. Stone, X. Zheng, S. L. Suib, M.-C. Lin, Y. Liang and H. Dai, *Proc. Natl. Acad. Sci. U. S. A.*, 2019, **116**, 23915-23922.
54. Y. Mi, Y. Qiu, Y. Liu, X. Peng, M. Hu, S. Zhao, H. Cao, L. Zhuo, H. Li, J. Ren, X. Liu and J. Luo, *Adv. Funct. Mater.*, 2020, **30**, 2003438.
55. N. Han, Y. Wang, J. Deng, J. Zhou, Y. Wu, H. Yang, P. Ding and Y. Li, *J. Mater. Chem. A*, 2019, **7**, 1267-1272.
56. X. Chen, H. Chen, W. Zhou, Q. Zhang, Z. Yang, Z. Li, F. Yang, D. Wang, J. Ye and L. Liu, *Small*, 2021, **17**, 2101128.
57. C. Cao, D.-D. Ma, J.-F. Gu, X. Xie, G. Zeng, X. Li, S.-G. Han, Q.-L. Zhu, X.-T. Wu and Q. Xu, *Angew. Chem., Int. Ed.*, 2020, **59**, 15014-15020.
58. S.-F. Leung, H.-C. Fu, M. Zhang, A. H. Hassan, T. Jiang, K. N. Salama, Z. L. Wang and J.-H. He, *Energy Environ. Sci.*, 2020, **13**, 1300-1308.
59. N. Han, Y. Wang, H. Yang, J. Deng, J. Wu, Y. Li and Y. Li, *Nat. Commun.*, 2018, **9**, 1320.